

Magnetic Energy and Helicity in Two Emerging Active Regions in the Sun

Y. Liu¹, P. W. Schuck²

ABSTRACT

The magnetic energy and relative magnetic helicity in two solar active regions AR11072 and AR11158 during their emergence are studied. They are computed by integrating over time, the energy- and relative helicity-fluxes across the photosphere. The fluxes consist of two components: one from photospheric tangential flows that shear and braid field lines (shear-term); the other from normal flows that advect magnetic flux into the corona (emergence-term). For these active regions (1) relative magnetic helicity in the active-region corona is mainly contributed by the shear-term; (2) helicity fluxes from emergence-term and shear-term have the same sign; (3) magnetic energy in the corona (including both potential energy and free energy) is mainly contributed by emergence-term; and (4) energy fluxes from emergence-term and shear-term evolved consistently in phase during the entire flux emergence course. We also examine the apparent tangential velocity derived by tracking field-line footpoints using a simple tracking method. It is found that this velocity is more consistent with tangential plasma velocity than with the flux transport velocity, which agrees with the conclusion in Schuck (2008).

Subject headings: Sun: active region—Sun: magnetic field—Sun: helicity and energy

1. Introduction

Magnetic energy and helicity in solar active regions are two volume integrated ideal MHD invariants that describe how energetic and complex an active region is. Computation of those quantities is challenging. Energy estimated from the modeled non-linear force-free

¹W. W. Hansen Experimental Physics Laboratory, Stanford University, Stanford, CA94305-4085

²Space Weather Laboratory, Code 674, Heliophysics Science Division, NASA Goddard Space Flight Center, Greenbelt, MD 20771

field computed from observational vector magnetic field on solar surface, for example, sometimes yields very unrealistic results (DeRosa et al. 2009). One reason is that the boundary data used are from the photosphere where the field is not force-free (Metcalf et al. 1995). Measurement of vector magnetic field in the chromosphere, where the field is close to force free, is very rare. Another way to estimate magnetic energy is based on Virial theorem (Metcalf et al. 2006). But it again requires that the vector field on the low-boundary be force-free. Estimating magnetic helicity is also difficult. Magnetic helicity in a volume V is defined by $H = \int_V \mathbf{A} \cdot \mathbf{B} dv$, where \mathbf{B} is magnetic field, and vector potential \mathbf{A} satisfies $\mathbf{B} = \nabla \times \mathbf{A}$. Thus, estimating helicity not only requires information of magnetic field but also vector potential in the volume. Helicity is physically meaningful (gauge invariant) only when no magnetic flux penetrates the surfaces of the volume V . For active regions in solar atmosphere, this condition is obviously not satisfied because magnetic flux penetrates the photosphere. For this case, one can use a relative measure of helicity, which is “topologically meaningful and gauge-invariant” (Berger & Field 1984). This relative magnetic helicity (for simplicity, hereafter we use magnetic helicity to refer to relative magnetic helicity) in a volume can be defined by subtracting the helicity of potential field \mathbf{B}_p in the volume that has the same vertical field on the photosphere. Computing this quantity has proved to be challenging (Klimchuk & Canfield 1994; Régnier & Canfield 2006). Alternatively, one can integrate over time energy- and helicity-fluxes across solar surface to estimate energy and helicity stored in an active region. Accurate estimate of the coronal energy and helicity requires that the computation be done from very beginning of emergence of the active region.

Magnetic helicity flux across a surface S is expressed by (Berger 1984),

$$\left. \frac{dH}{dt} \right|_S = 2 \int_S (\mathbf{A}_p \cdot \mathbf{B}_t) V_{\perp n} dS - 2 \int_S (\mathbf{A}_p \cdot \mathbf{V}_{\perp t}) B_n dS, \quad (1)$$

where, \mathbf{A}_p is vector potential of the potential field \mathbf{B}_p , \mathbf{B}_t and B_n denote the tangential and normal magnetic fields, and $\mathbf{V}_{\perp t}$ and $V_{\perp n}$ are the tangential and normal components of velocity \mathbf{V}_{\perp} , the velocity perpendicular to magnetic field lines. The integral is done over the surface. When applied to the Sun, it indicates that the magnetic helicity in the corona comes from the twisted magnetic flux tubes emerging from the solar interior into the corona (first term; emergence-term hereafter), and is generated by shearing and braiding the field lines by the tangential motions on the solar surface (second term; shear-term hereafter) (see, e.g., Berger 1984; Kusano et al. 2002; Nindos et al. 2003; Pevtsov et al. 2003; Pariat et al. 2005; Démoulin 2007). If the surface S is planar, this equation can be re-written as (Pariat et al. 2005),

$$\left. \frac{dH}{dt} \right|_S = \frac{1}{2\pi} \int_S \int_{S'} ds ds' \hat{\mathbf{n}} \cdot \frac{\mathbf{x} - \mathbf{x}'}{|\mathbf{x} - \mathbf{x}'|^2} \times \{ \mathbf{B}_t(\mathbf{x}) V_{\perp n}(\mathbf{x}) B_n(\mathbf{x}') - \mathbf{B}_t(\mathbf{x}') V_{\perp n}(\mathbf{x}') B_n(\mathbf{x}) \}$$

$$-\frac{1}{2\pi} \int_S \int_{S'} ds ds' \hat{\mathbf{n}} \cdot \frac{\mathbf{x} - \mathbf{x}'}{|\mathbf{x} - \mathbf{x}'|^2} \times \{[\mathbf{V}_{\perp t}(\mathbf{x}) - \mathbf{V}_{\perp t}(\mathbf{x}')] B_n(\mathbf{x}) B_n(\mathbf{x}')\}, \quad (2)$$

where \mathbf{x} and \mathbf{x}' represent two photospheric positions, and $\hat{\mathbf{n}}$ is the surface normal pointing into the corona.

Similarly, magnetic energy (Poynting) flux can be expressed by (Kusano et al. 2002),

$$\left. \frac{dE}{dt} \right|_S = \frac{1}{4\pi} \int_S B_t^2 V_{\perp n} dS - \frac{1}{4\pi} \int_S (\mathbf{B}_t \cdot \mathbf{V}_{\perp t}) B_n dS. \quad (3)$$

Again, energy flux across solar surface comes from emergence of twisted magnetic tubes from solar interior (first term; emergence-term) and is generated by shearing magnetic field lines due to tangential motions on the surface (second term; shear-term).

When using Equations (1) and (3) to compute magnetic helicity and energy in localized volumes of the corona such as above a computational region in the photosphere we need to additionally ensure or assume connectivity of the footpoints when the data are only available at the lower boundary, the photosphere—no field lines should leave through the sides of localized volume in the corona and return the surface of the Sun outside of computational region in the photosphere. Data needed for this calculation are vector magnetic and velocity fields on the photosphere. Measurement of vector magnetic field on the photosphere has been made for many years, but, to our best knowledge, there are no direct measurements of vector velocity field on the photosphere so far. Recently, a great progress has been made to infer vector velocity field in the photosphere using time-series vector magnetic field measurements (e.g. Kusano et al. 2002; Welsch et al. 2004; Longcope 2004; Georgoulis & LaBonte 2006; Schuck 2008). The input for those algorithms is the time-series vector magnetic field data on solar surface (usually the photosphere). As the temporal derivatives of the magnetic field are involved in those methods, vector magnetic field data with continuous observation, high cadence and consistency of data quality are required. These requirements limit the applications of those models to observations in the past because most vector field data with a reasonable cadence were taken by the ground-based magnetographs at various observatories where local night and bad weather led to substantial data gaps, and seeing and other conditions further caused inconsistency of data quality and produced non-solar motions in the image sequence. Thus only a few attempts were made using these equations to study the energy- and helicity-buildup in solar active regions using observational data (e.g. Kusano et al. 2002; Nindos et al. 2003; Yamamoto et al. 2005; Yamamoto & Sakurai 2009). For example, Kusano et al. (2002) decomposed the helicity flux into the emergence-term and the shear-term, and studied their contributions to the helicity in the corona in an emerging active region. The data used was a combination of the line-of-sight magnetograms taken by the *Michelson Doppler Imager* (MDI; Scherrer et al. 1995) and the vector magnetic field

data taken by the vector magnetograph at the National Astronomical Observatory of Japan (NAOJ). Yamamoto et al. (2005); Yamamoto & Sakurai (2009) used the same method to analyze more active regions. Since the vector magnetic field data used in those studies were taken by a ground-based magnetograph, they possess the aforementioned caveats. A test with MHD data further showed that the method they used might be insensitive to capture the helicity flux (Welsch et al. 2007). Therefore, it is necessary to revisit this topic using better algorithms and better observational data. This is one purpose for this study.

There is another approach proposed to study helicity and energy fluxes across the photosphere. By introducing the flux transport velocity \mathbf{U} ($\mathbf{U} = \mathbf{V}_{\perp t} - \frac{V_{\perp n}}{B_n} \mathbf{B}_t$), Démoulin & Berger (2003) simplified the forms of Equations (1) and (3) to be,

$$\left. \frac{dH}{dt} \right|_S = -2 \int_S (\mathbf{A}_p \cdot \mathbf{U}) B_n dS, \quad (4)$$

and,

$$\left. \frac{dE}{dt} \right|_S = -\frac{1}{4\pi} \int_S (\mathbf{B}_t \cdot \mathbf{U}) B_n dS. \quad (5)$$

They further argued geometrically that the apparent tangential velocity derived by tracking footpoints of normal magnetic field is in fact the flux transport velocity (DB03-hypothesis hereafter). This allows helicity flux to be computed from line-of-sight magnetograms and the aforementioned tracking velocity on the surface. Thus it suggested a feasible way to study magnetic helicity in active regions because high-quality line-of-sight magnetic field measurements with reasonable cadence have been available for many years by, for example, the MDI and the *Global Oscillation Network Group* (GONG). In fact, many studies have been carried out since then (see Démoulin (2007); Démoulin & Pariat (2009) for reviews). For example, using this hypothesis, Zhang et al. (2012) decomposed the helicity flux into the shear-term and the emergence-term, and discussed their contributions to the helicity accumulated in the corona. However, the validity of this hypothesis has been questioned (Schuck 2008; Ravindra et al. 2008). Examining this hypothesis is another purpose of this study.

Full disk field-of-view, continuous observation coverage, high temporal and spatial resolutions, and consistent data quality, these specifications of observational data taken by the *Helioseismic and Magnetic Imager* (HMI; Scherrer et al. 2012; Schou et al. 2012) on-board the *Solar Dynamics Observatory* (SDO; Pesnell et al. 2012) allow us to study magnetic energy- and helicity-injection into active-region corona, especially their buildup and evolution during flux emergence because full disk measurement provides data that catch very beginning of emergence of active regions. In this paper, using HMI vector magnetic field data, we decompose the energy- and helicity-fluxes into the shear-term and the emergence-term and study

the roles they play in energy and helicity buildup in the corona in active regions during their emergence. And with the observational data, we test the DB03-hypothesis.

The paper is organized as follow. In Section 2, we briefly describe HMI instrument, data reduction, helicity flux computation, and the active regions chosen for this study. Analysis and result are presented in Section 3. Test of DB03-hypothesis is in Section 4. We conclude this work in Section 5.

2. HMI Data Reduction, Helicity Flux, and Two Emerging Active Regions

2.1. Data Reduction

We use vector magnetic field data taken by HMI. The HMI instrument is a filtergraph with a full disk coverage at 4096×4096 pixels. The spatial resolution is about 1" with a 0.5" pixel size. The width of the filter profiles is 76 mÅ. The spectral line is the FeI 6173Å absorption line formed in the photosphere (Norton et al. 2006). There are two CCD cameras in the instrument, the “front camera” and the “side camera.” The front camera acquires the filtergrams at 6 wavelengths along the line FeI 6173Å in two polarization states with 3.75 seconds between the images. It takes 45 seconds to acquire a set of 12 filtergrams. This set of data is used to derive the Dopplergrams and the line-of-sight magnetograms. The side camera is dedicated to measuring the vector magnetic field. It takes 135 seconds to obtain the filtergrams in 6 polarization states at 6 wavelength positions. The Stokes parameters [I, Q, U, V] are computed from those measurements, and are further inverted to retrieve the vector magnetic field. In order to suppress the p-modes and increase the signal-to-noise ratio, usually the Stokes parameters are derived from the filtergrams averaged over certain time. Currently the average is done with 720-second measurements. They are then inverted to produce the vector magnetic field using an inversion algorithm Very Fast Inversion of the Stokes Vector (VFISV). VFISV is a Milne-Eddington (ME) based approach developed at High Altitude Observatory (HAO) (Borrero et al. 2011). The 180° degree ambiguity of the azimuth is resolved based on the “minimum energy” algorithm (Metcalf 1994; Metcalf et al. 2006; Leka et al. 2009). With significant improvements in the original algorithm, the disambiguation module for automatic use in *HMI-AIA Joint Science Operations Center* (JSOC) is implemented by the NorthWest Research Associates (NWRA) at Boulder. The patches of the active regions are automatically identified and bounded by a feature recognition model (Turmon et al. 2010), and the disambiguated vector magnetic field data of active regions are deprojected to the heliographic coordinates. Here we use Lambert (cylindrical equal area) projection method for the deprojection. For small area like a normal active region, difference in the deprojected maps from different projection

methods is very small (R. Bogart, 2011, private communication). The vector velocity field in the photosphere is derived from the Differential Affine Velocity Estimator for Vector Magnetograms (DAVE4VM; Schuck 2008) that is applied to the time-series deprojected, registered vector magnetic field data. The window size used in DAVE4VM is 19 pixels, which is selected by examining slope, Pearson linear correlation coefficient, and Spearman rank order between $\nabla_h \cdot (V_n \mathbf{B}_t - \mathbf{V}_t B_n)$ and $\delta B_n / \delta t$, where V_n and \mathbf{V}_t are normal and tangential velocities, and B_n and \mathbf{B}_t are normal and tangential magnetic fields, as suggested by Schuck (2008). This velocity is further corrected by removing the irrelevant field-aligned plasma flow by,

$$\mathbf{V}_\perp = \mathbf{V} - \frac{\mathbf{V} \cdot \mathbf{B}}{B^2} \mathbf{B}, \quad (6)$$

where \mathbf{V}_\perp is velocity perpendicular to magnetic field line, and \mathbf{V} is the velocity derived by DAVE4VM. Velocity \mathbf{V}_\perp is used to compute energy and helicity fluxes in this paper. Detailed information on HMI vector field data processing can be found in Hoeksema et al. (2012) and Sun et al. (2012).

2.2. Helicity Flux

Two issues are related to the helicity flux: (1) how to compute helicity flux, and (2) how to interpret helicity fluxes that are associated with tangential and vertical flows.

2.2.1. Helicity flux computation

Magnetic helicity flux across the photosphere can be calculated from Equations (1) or (2). The integral was done over an area of interest (usually it encloses an active region). Vector potential \mathbf{A}_p of the potential field on the photosphere is uniquely determined by the observed photospheric vertical magnetic field and Coulomb gauge by equations (Berger 1997; Berger & Ruzmaikin 2000),

$$\nabla \times \mathbf{A}_p \cdot \hat{\mathbf{n}} = B_n, \nabla \cdot \mathbf{A}_p = 0, \mathbf{A}_p \cdot \hat{\mathbf{n}} = 0. \quad (7)$$

Pariat et al. (2005) showed that the helicity flux density in Equation (1) has spurious signals. Theoretically, these false signals are canceled out completely when the total helicity flux is computed by integrating the flux density over the whole region. However, Pariat et al. (2006) found that the helicity flux computed from Equations (1) and (2) could yield an up to 15% difference, and they attributed it primarily to the fake signals that the flux density produces. They also suggested that the noise in the data also makes some contribution.

Actually, this difference is caused by the boundary condition chosen to compute the helicity flux density. They used a periodic Green’s function via the Fast Fourier Transform (FFT) to compute helicity flux via Equation (1) and a free-space Green’s function via Equation (2). This difference vanishes completely when the boundary condition on Green’s function is consistently chosen (Liu & Schuck 2012). Given that the actual data set is a remapped cutout of the spherical Sun, it is not clear which method FFT, free-space Green’s function, or finite difference solution with Dirichlet boundary conditions (Schuck 2008) gives a more accurate estimate for total helicity flux computation. A 15% difference is well within the error from the noise of the vector magnetic field data that is estimated in Section 3.1.1. Therefore we use FFT to compute the helicity flux in this paper.

2.2.2. Interpretation of helicity fluxes related to tangential and normal flows.

As described in Section 1, the magnetic helicity in the corona comes from the twisted magnetic flux tubes emerging from the solar interior into the corona (the emergence-term), and is generated by shearing and braiding the field lines by the tangential motions on the solar surface (the shear-term). The emergence-term includes the helicity in the twisted magnetic flux tubes that emerge into the corona and the mutual helicity between the pre-existing magnetic field and this newly emerged field. Similarly, the shear-term includes helicity generated by shearing the field lines and the mutual helicity between the shearing field and the background field due to change of field geometry. Interpretation of $\mathbf{V}_{\perp n}$ -term that is related with emergence and $\mathbf{V}_{\perp t}$ -term that is related with shear motion on the surface was explicitly stated in Berger (1984) (see also Kusano et al. 2002; Démoulin & Berger 2003; Nindos et al. 2003; Pevtsov et al. 2003; Pariat et al. 2005; Démoulin 2007).¹

2.3. Two Emerging Active Regions: AR 11072 and AR 11158

Two active regions, AR 11072 and AR 11158, are chosen for this study. AR 11072 was a simple active region with a bipolar structure of magnetic field. It began to emerge on 20 May 2010 at the southern hemisphere (S15E48). No C-class or above flares occurred in this region during its disk passage. AR 11158, on the other hand, was an active region with complex magnetic field configuration. It started to emerge on 10 February 2011 at the

¹Using both MHD data in Welsch et al. (2007) and HMI data, it is possible to show that the separation of the helicity fluxes into two terms gives identical results whether computed via Equation (1) or Equation (2) (Liu & Schuck 2012)

southern hemisphere (S20E60), and produced several major flares during its disk passage. Its flare activity and magnetic evolution were described and analyzed in Sun et al. (2012); Wang et al. (2012); Jing et al. (2012).

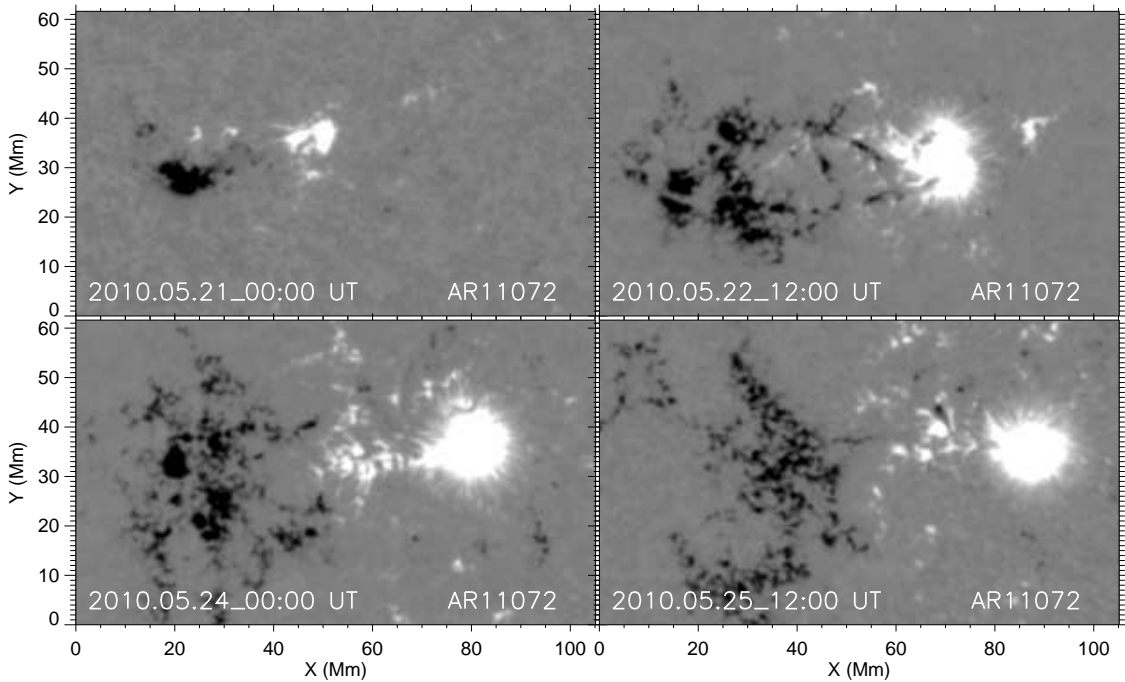


Fig. 1.— Evolution of normal magnetic field of AR 11072. White and black in the images refer to positive and negative fields. All images are scaled to $\pm 800.0 \text{ Mx cm}^{-2}$.

3. Results

3.1. AR 11072

Fig. 1 presents snapshots of normal magnetic field in AR 11072, showing its emergence and evolution. The leading and following fields emerged and moved apart each other, developing a typical bipolar active region: compact leading polarity (positive) and fragmented following polarity (negative). Fig. 2 displays vector magnetic field at 12:00 UT 22 May 2010. It looks fairly potential. Velocity \mathbf{V}_\perp is shown in Fig. 3. Tangential velocity (left panel) successfully reproduces the evolutionary characteristics in this region seen in a magnetic field movie: the leading and following fields separated each other, and the leading polarity patch appeared to rotate counter-clockwisely. Normal velocity (right panel) reveals strong upflows at the middle of the active region where the flux emergence took place.

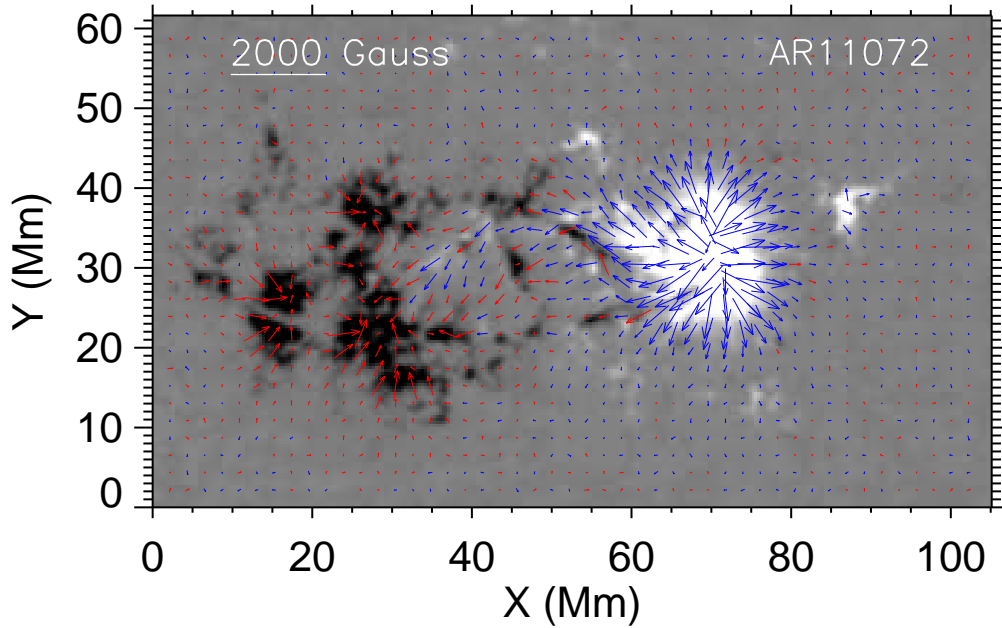


Fig. 2.— Vector magnetic field of AR11072 at 12:00 UT 22 May 2010. The active region was at S16W00. The image is normal field with positive field in white and negative in black. It is scaled to $\pm 800.0 \text{ Mx cm}^{-2}$. The arrows represent tangential field. Blue (red) arrows indicate that the normal fields at those pixels are positive (negative).

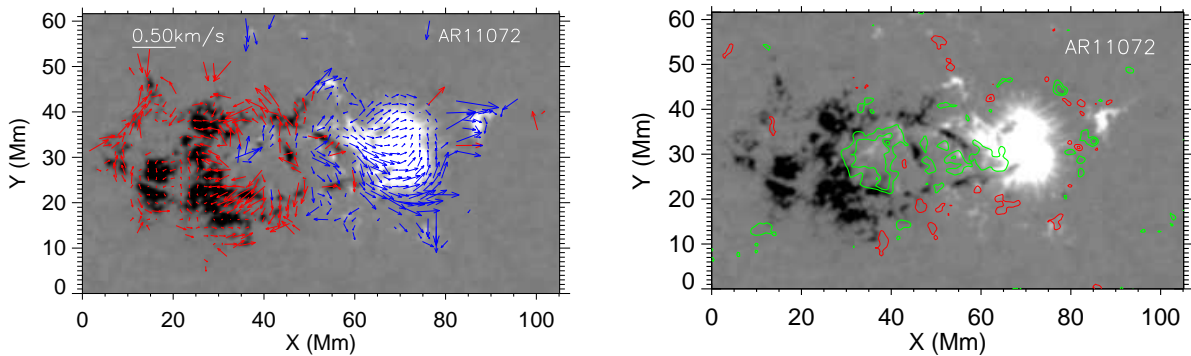


Fig. 3.— Velocity field \mathbf{V}_\perp of AR11072 at 12:00 UT 22 May 2010. The images are normal magnetic field saturated at $\pm 800.0 \text{ Mx cm}^{-2}$. The arrows in the left panel refer to tangential velocity, and the contours in the right refer to normal velocity with upflows in green and downflow in red. Blue (red) arrows indicate that the normal magnetic fields in the pixels are positive (negative). Only tangential velocity at the pixels where the normal field is greater than 40.0 Mx cm^{-2} is plotted. The contour levels are $\pm 0.12, \pm 0.24, \pm 0.48 \text{ km s}^{-1}$.

Emergence and evolution of the active region are also illustrated in the top panel of Fig. 4. The blue, red and black curves are temporal profiles of positive, negative, and unsigned magnetic fluxes from 20–26 May 2010. Unsigned flux is defined to be the summation of positive flux and absolute value of negative flux. It is seen that the active region began to emerge at 07:00 UT 21 May, and lasted for 40 hours (from hours 15–55). Basically, the magnetic flux in this region was balanced during the course of emergence. The total flux reached 8×10^{21} Mx. The net flux was below 10% of the total unsigned flux in this 6-day period. Net flux is the summation of positive and negative fluxes. Obviously, any flux imbalance is caused by either limitations in the field of view or measurement limitations and errors. Flux balance is a necessary but not sufficient condition for connectivity of the footpoints. And matched footpoints closed field regions is necessary for an accurate assessment of the Poynting and helicity fluxes through the photosphere into the near corona.

3.1.1. Magnetic Helicity in AR 11072

Temporal profiles of helicity fluxes across the photosphere are plotted in the middle panel of Fig. 4. Red and blue curves represent the helicity fluxes from $\mathbf{V}_{\perp t}$ (shear-helicity flux hereafter) and from $\mathbf{V}_{\perp n}$ (emergence-helicity flux hereafter), respectively. Recall that $\mathbf{V}_{\perp t}$ and $\mathbf{V}_{\perp n}$ are tangential and normal components of \mathbf{V}_{\perp} . A 2-hour running average was applied in order to show their average temporal behavior. Violet and light blue curves refer to the accumulated helicities from shear- and emergence-helicity fluxes, respectively. The accumulated helicity plotted here is the integral of the helicity flux over time that is deemed to be the helicity stored in the corona. Black curve is total helicity, summation of both terms. Uncertainties of the shear- and emergence-helicity fluxes were also reported by the black and green error-bars. They were estimated by conducting a Monte Carlo experiment. In this experiment, we randomly added noise to three components of vector magnetic field, and repeated the vector velocity and helicity flux computations. The noise added has a Gaussian distribution, and the width (σ) of the Gaussian function is 100 Gauss, roughly the noise level of vector magnetic field (Hoeksema et al. 2012). This test was repeated 200 times. The original error, the root mean square (RMS; σ) of these 200 experiments, was then adjusted by that 2-hour running average, and finally plotted by error-bars in Fig. 4. Here we only plot errors at several representative instants in order to better show the results. Averaging the five original errors of shear-helicity flux between hours 35–65, where the shear-helicity flux is significant, yields 23%, greater than the maximum difference (15%) of helicity fluxes computed via Equation (1) and (2) reported in Pariat et al. (2006). The evolutionary characteristics of the fluxes are well above the errors. The shear-helicity flux was dominant. It was high during flux emergence and quickly approached to zero after

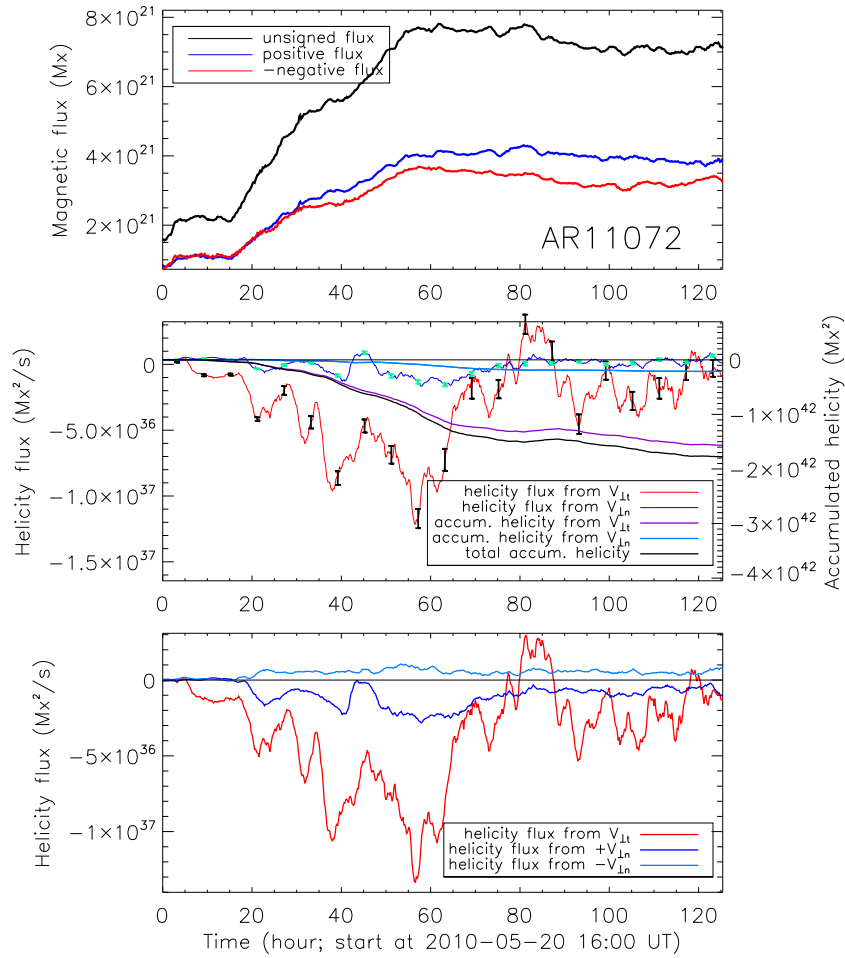


Fig. 4.— Top: Temporal profiles of magnetic flux in AR 11072. Black, blue and red curves refer to unsigned, positive and absolute negative fluxes, respectively. The curves start at 16:00 UT 20 May 2010. Middle: temporal profiles of magnetic helicity of AR 11072. Red and blue curves represent helicity fluxes across the photosphere from shear- and emergence-terms, respectively. $1\text{-}\sigma$ error is presented by the black and green error-bars, which are plotted only at several representative times. Violet and light blue curves refer to accumulated helicities in the corona from shear- and emergence-terms. The black curve is total accumulated helicity (summation of these two terms). Bottom: temporal profiles of helicity flux across the photosphere from shear-term (red), upflows (blue) and downflows (light blue).

the emergence significantly reduced. Emergence-helicity flux, on the other hand, remained very low level in the entire six-day time period. Both helicities were negative. This is

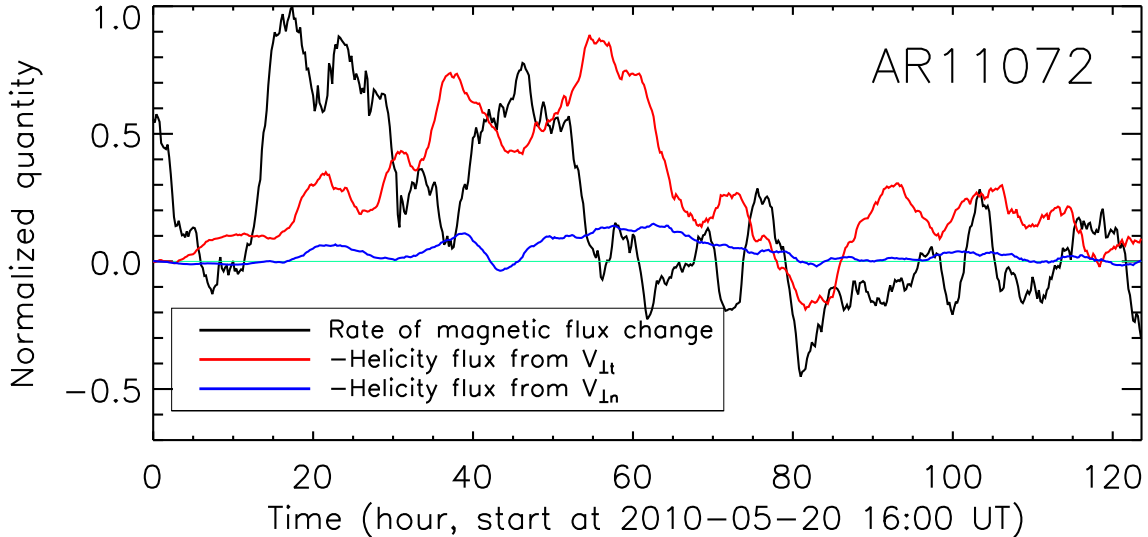


Fig. 5.— Six-day temporal profiles of change rate of the photospheric unsigned magnetic flux (black), $-1 \times$ (helicity fluxes) from shear-term (red) and from emergence-term (blue), in the active region AR 11072. A four-hour running average is applied to the data. They are normalized by the maximum values of flux change rate and total helicity flux in this time period, respectively.

opposite to the so-called “hemisphere rule,” which predicts that active regions in southern hemisphere have positive helicity. The total helicity accumulated in the corona in this six-day period was $-1.7 \times 10^{42} \text{ Mx}^2$. Among that, 88% was contributed by shear-term. We further separated emergence-helicity flux into two components: helicity flux from upflows (upflow-helicity flux) and from downflows (downflow-helicity flux). Their temporal profiles are shown in the bottom panel of Fig. 4, together with the profile of shear-helicity flux. The upflow- and downflow-helicity fluxes had different signs, while upflow-helicity flux had the same sign as the shear-helicity flux. Both fluxes were very low. The upflow-helicity flux is from the twisted/sheared field emerging from interior into the corona and the mutual helicity between this emerging field and the pre-existed field.

To better examine relationship between magnetic flux emergence and helicity injection, we plot in Fig. 5 the temporal profiles of change rate of the total unsigned flux (black), $-1 \times$ shear-helicity flux (red) and $-1 \times$ emergence-helicity flux (blue). A four-hour running average was applied. Change rate of total unsigned flux is normalized by its maximum value, while both helicity fluxes are normalized by the maximum of the summation of them. There were two quick emergence processes in the early 60 hours, hours 10–30 and hours 40–55. The

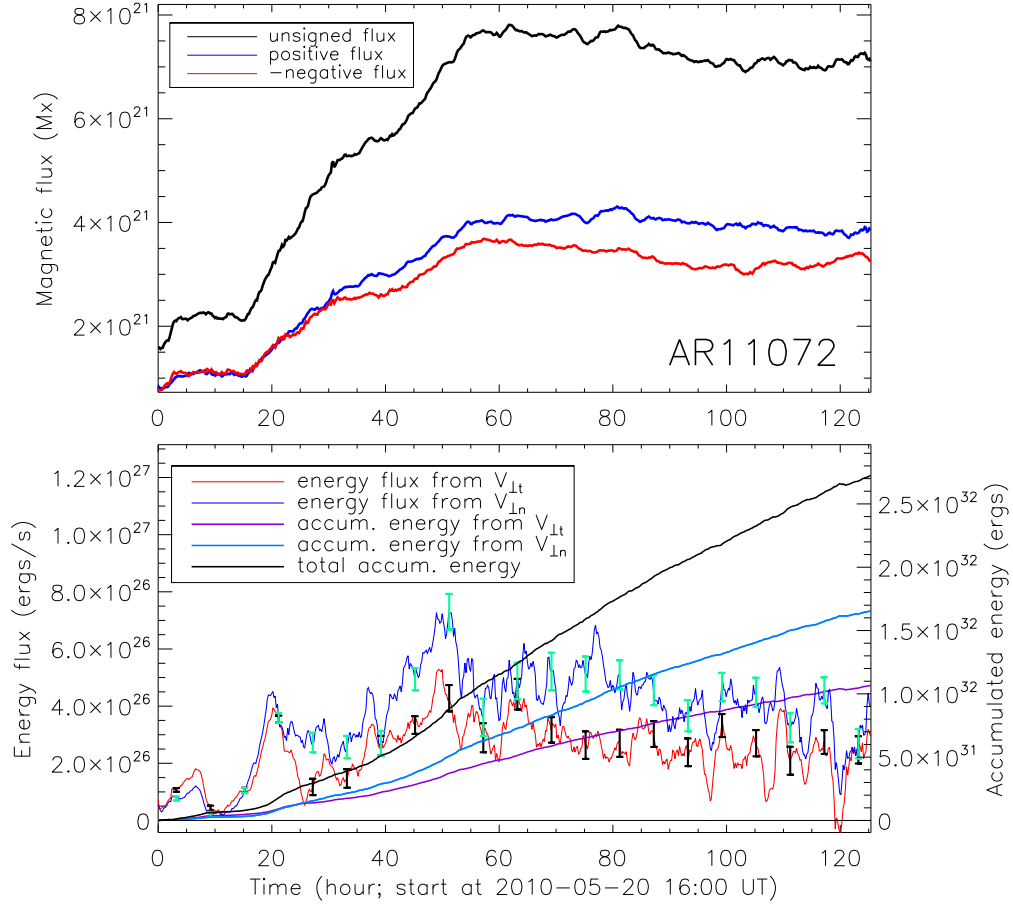


Fig. 6.— Top: same as in the top panel of Fig. 4. Bottom: temporal profiles of energy fluxes from shear-term (red) and emergence-term (blue), respectively. $1\text{-}\sigma$ error is presented by the black and green bars. Violet and light blue curves refer to the accumulated energy in the corona from shear-term and emergence-term. Black curve is the sum of them. The accumulated energy here is the integral of the energy flux over time.

emergence became much less significant since then. It also appeared to have a delay between flux emergence and helicity injection, which was reported previously in Tian & Alexander (2008). To determine this delay numerically, we shifted the shear-helicity flux and computed the correlation coefficient between the shifted helicity flux and the rate of magnetic flux change. The range for shift is ± 20 hours with a step of 0.2 hours. This analysis was applied to the raw data without applying that 2-hour running average. A 12.8-hour shift for the shear-helicity flux yields a maximum correlation coefficient, which is 0.32. This infers that there may be a phase lag of 12.8 hours between them. Besides this possible lag, the flux emergence and the shear-helicity flux is well correlated: the shear-helicity flux was significant during emergence, and quickly approached to zero after about 70 hours when the emergence

significantly reduced. This indicates that the photospheric shear motion, which produced most helicity in the corona, was tightly related with flux emergence.

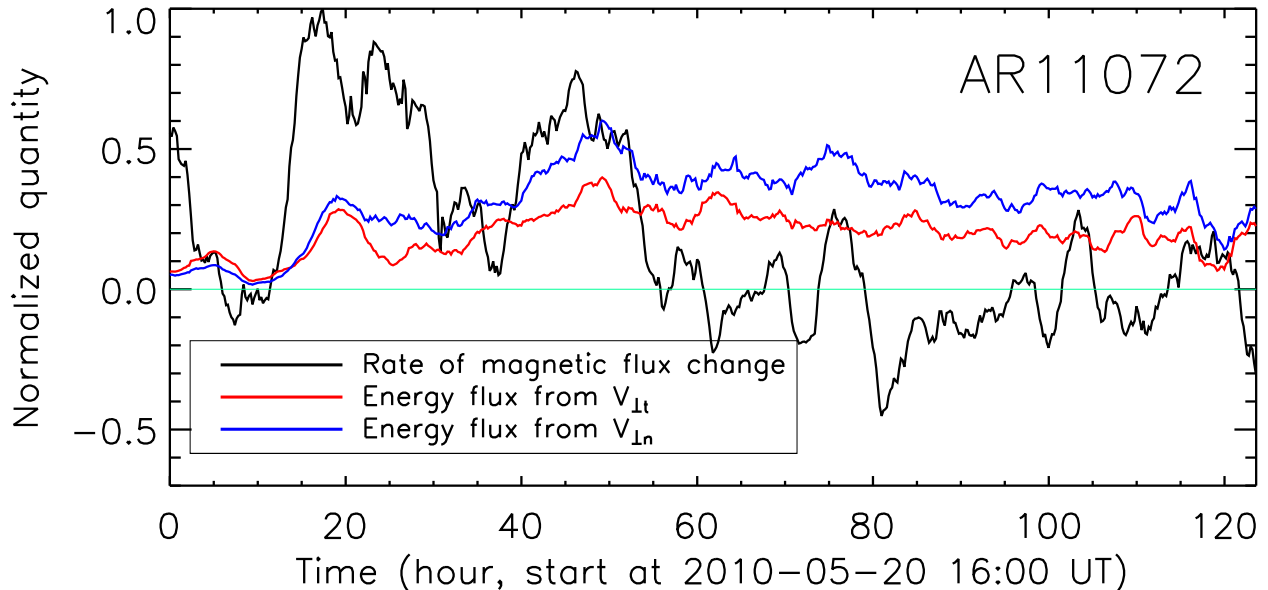


Fig. 7.— Similar as in Fig. 5, but red and blue curves refer to temporal profiles of energy fluxes from shear- and emergence-terms, respectively.

3.1.2. Magnetic Energy in AR11072

Magnetic energy in AR11072 is also calculated using Equation (3). The black, blue and red curves in the top panel of Fig. 6 refer to unsigned, positive and negative fluxes, respectively. The bottom panel shows the energy fluxes from $\mathbf{V}_{\perp t}$ (red; shear-energy flux hereafter) and $V_{\perp n}$ (blue; emergence-energy flux hereafter), respectively. A 2-hour running average was applied. Violet and light blue curves refer to integrals of the energy fluxes over time, representing the magnetic energy accumulated in the corona. The black curve is the summation of them. $1\text{-}\sigma$ errors are plotted at several representative times for shear-energy flux (black) and for emergence-energy flux (green), respectively. Again, they were obtained by conducting a Monte Carlo experiment, as same as that for helicity fluxes. The total energy accumulated in the corona in the six-day period was about 2.8×10^{32} ergs. Emergence-energy flux was dominant, contributing about 61% of the total energy, while shear-energy flux contributed 39%. Both fluxes had two obvious increases in the first 60 hours, consistent with the timing of flux emergence. This correlation is demonstrated clearly in a phase-relationship plot in Fig. 7, where black curve represents temporal profile of change rate of total unsigned

flux, red and blue curves refer to shear- and emergence-energy fluxes, respectively. The two increases coincided with the two significant flux emergence courses: one was from hours 10–30, and the other from hours 40–55. It also shows that both energy fluxes evolved consistently in phase, but the emergence-energy flux was higher than the shear-energy flux during the entire 6-day period. We did a correlation analysis between the energy injection and flux emergence, similar as that between the helicity injection and flux emergence. A 3-hour shift of the energy flux yields the maximum correlation coefficient. But it is very small, only 0.15. Another interesting feature in this figure is that, after the emergence significantly reduced, the normal flow still injected significant energy into the corona. This is illustrated by high emergence-energy flux after hour 60. The source of this energy injection was the upflows that surrounded the leading sunspot, as demonstrated in Fig. 8, where $\mathbf{V}_{\perp n}$ (left panel) and emergence-energy flux (right) are over-plotted in contours on the normal magnetic field. The data plotted here were taken at 12:00 UT 23 May 2010, after the flux emergence reduced greatly. Note that, although $\mathbf{V}_{\perp n}$ showed strong signals in some weak-field areas where magnetic field measurement is less reliable (left panel), the concentrations of the emergence-energy flux are actually in strong field areas (right panel). Thus, the strong $\mathbf{V}_{\perp n}$ in the weak field areas contributed much less emergence-energy flux. This is also shown by the small error bar at hour 68 in Fig. 6, where the error bar was estimated by conducting a Monte Carlo experiment by randomly adding noise to the magnetic field.

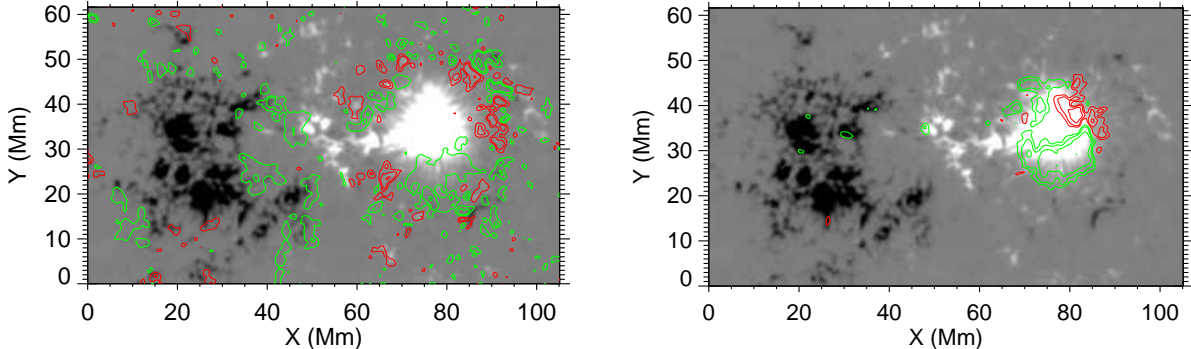


Fig. 8.— Left: The black-white image is the normal magnetic field of AR 11072 at 12:00 UT 23 May 2010, over-plotted in contours by $\mathbf{V}_{\perp n}$. The contour levels are ± 0.16 , ± 0.32 , ± 0.64 km s^{-1} with upflows in green and downflow in red. The image is saturated at ± 800 Mx cm^{-2} with positive field in white and negative field in black. Right: The image represents normal magnetic field, over-plotted in contour by emergence-energy flux density. The green and red contours refer to the positive and negative energy fluxes. The contour levels are $\pm 0.08 \times 10^{10}$, 0.16×10^{10} , and 0.24×10^{10} $\text{ergs cm}^{-2} \text{ s}^{-1}$.

3.2. AR 11158

Fig. 9 shows evolution of normal magnetic field in AR 11158 from 12–15 February 2011. It began to quickly emerge on 12 February 2011, and finally developed to become a complex, multipolar active region. Fig. 10 displays vector magnetic field at 19:48 UT 2011 February 14. Magnetic field was highly sheared along the polarity inversion line at the middle of the region. The apparent twisted magnetic fields in the negative sunspots were probably caused by the fast spinning of the sunspots. $\mathbf{V}_{\perp t}$ (arrows in the left panel of Fig. 11) revealed various flow patterns that were consistent with what were shown in the time-series magnetic field data: separation motion of the leading and following polarities, strong shear motions along the polarity inversion line, and the rotations in sunspots. Similar with that in AR 11072, the $\mathbf{V}_{\perp n}$ map (right panel of Fig. 11) exhibits strong upflows surrounding sunspots. Magnetic flux in this region was well balanced during its emergence, as shown in top panel of Fig. 12.

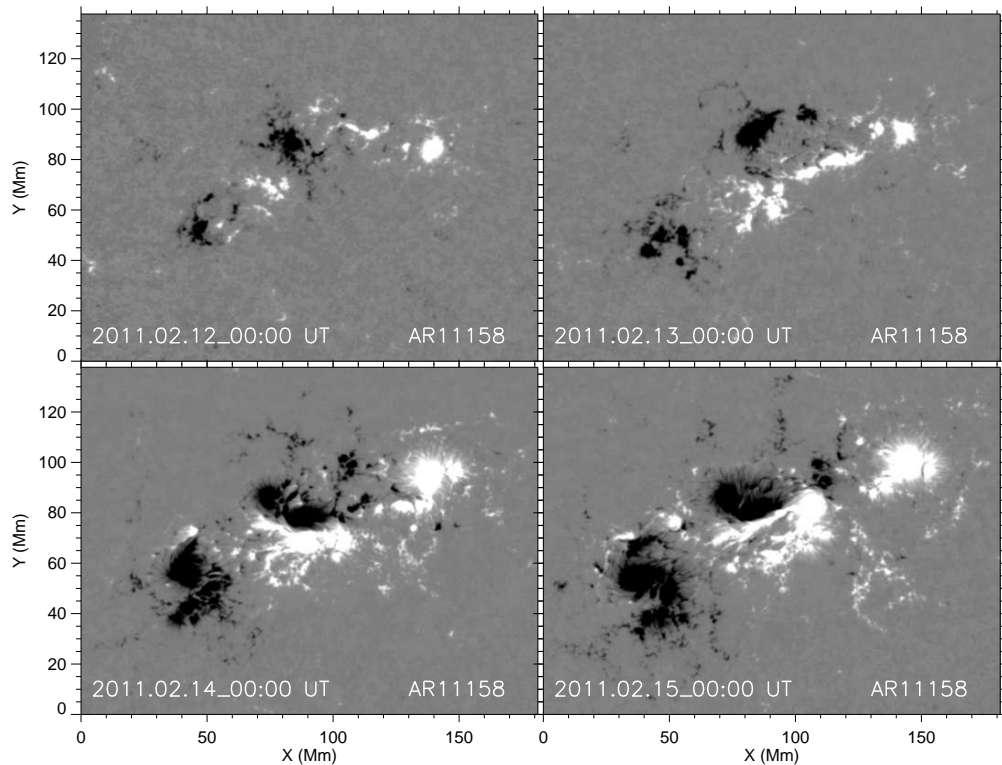


Fig. 9.— Evolution of normal magnetic field of AR 11158 from 12–15 February 2011. The images are saturated at $\pm 800 \text{ Mx cm}^{-2}$ with positive field in white and negative field in black.

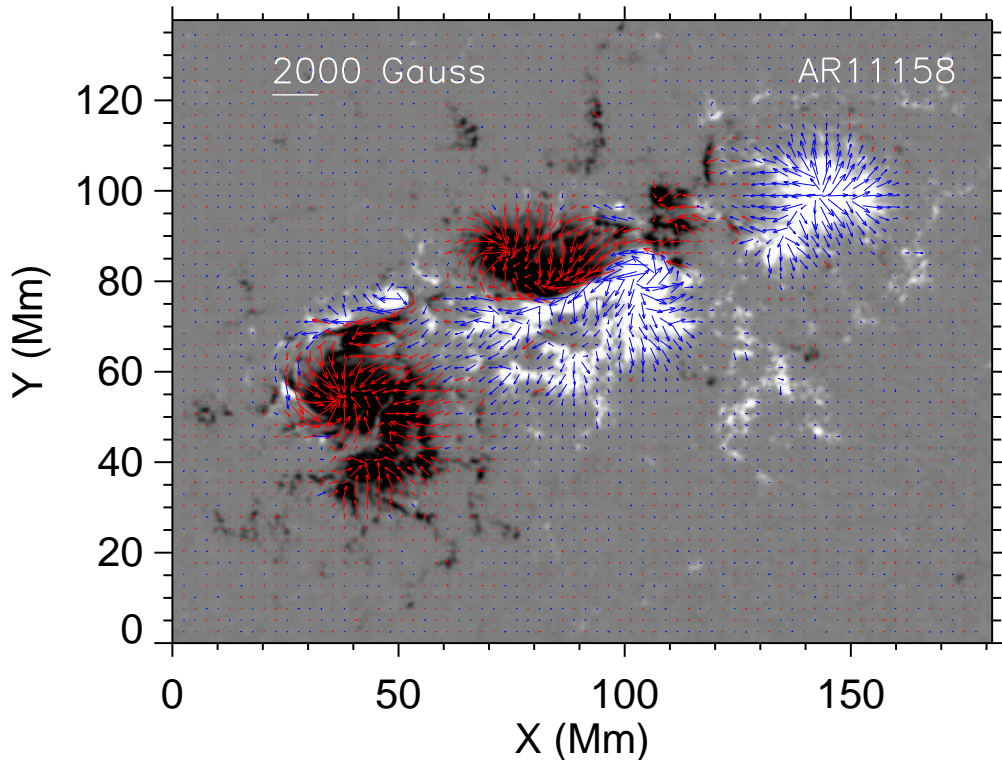


Fig. 10.— Vector magnetic field in AR11158 at 19:48 UT 14 February 2011 at S20W12. The image represents normal magnetic field with positive field in white and negative field in black. It is scaled to $\pm 800 \text{ Mx cm}^{-2}$. The arrows refer to tangential field. Blue (red) arrows indicate that the normal fields at those pixels are positive (negative).

3.2.1. Magnetic Helicity in AR 11158

Temporal profiles of magnetic helicity in this region are plotted in the middle panel of Fig. 12. The shear-helicity flux dominated in this five-day time period, while the emergence-helicity flux was moderately low. The helicities in the corona injected by both fluxes were positive, which followed the “hemispheric rule.” Total helicity accumulated in the corona in this five-day time period reached $1.8 \times 10^{43} \text{ Mx}^2$, of which shear-term contributed about 66% and emergence-term about 34%. Same as for AR11072, uncertainties of shear- and emergence-helicity fluxes were obtained by conducting a Monte Carlo experiment. We also separated emergence-helicity flux into upflow- and downflow-helicity fluxes. They are plotted in the bottom panel, together with shear-helicity flux. Upflows and downflows injected helicity of opposite signs into the corona, while the helicity from upflows has the same sign as that from tangential velocity. The helicity flux from upflows was moderate, but still lower than that from the shear-term.

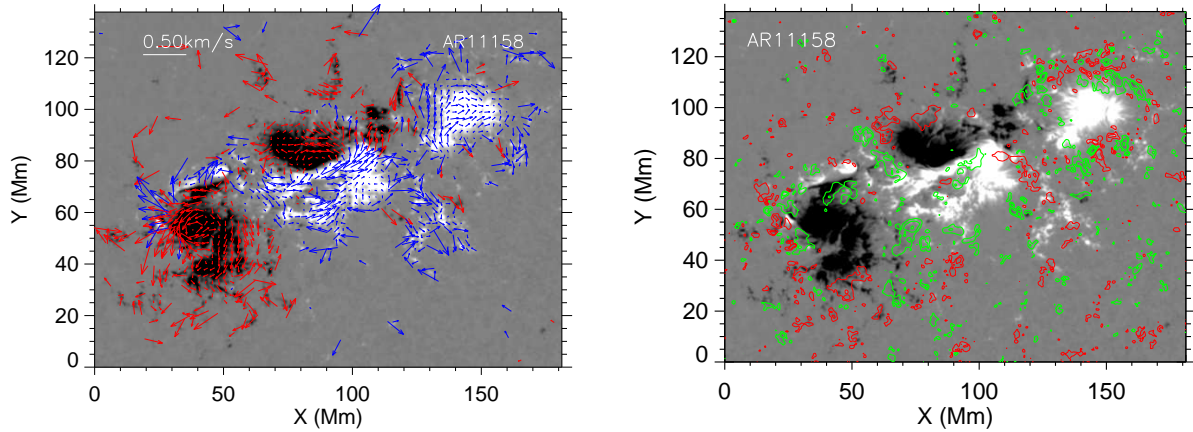


Fig. 11.— Same as Fig.3 but for AR 11158. The data were taken at 19:48 UT 14 February 2011 when the region was at S20W12. The images are normal magnetic field saturated at $\pm 800.0 \text{ Mx cm}^{-2}$. The arrows in the left panel refer to tangential velocity, and the contours in the right panel refer to normal velocity with upflows in green and downflow in red. The contour levels are $\pm 0.09, \pm 0.18, \pm 0.36 \text{ km s}^{-1}$.

Fig. 13 shows relationship between the flux emergence and helicity flux. The shear-helicity flux was dominant. Both shear- and emergence-helicity fluxes were low during the main flux emergence between hours 15–40, and the shear-helicity flux significantly increased afterwards. A 4.8-hour shift for the shear-helicity flux yields a maximum correlation coefficient between this flux and the rate of magnetic flux change, but the coefficient is only 0.30.

3.2.2. Magnetic Energy in AR 11158

Fig. 14 shows temporal profiles of energy fluxes. The uncertainties of shear- and emergence-energy fluxes were obtained by conducting a Monte Carlo test. The emergence-energy flux was again dominant, contributing 62% of total energy, while the shear-energy flux contributed about 38%. The total energy accumulated in the corona reached 1.3×10^{33} ergs in the five-day period. Both fluxes evolved consistently in phase in the entire flux emergence course, as demonstrated in Fig. 15. No phase shift is found between energy injection and magnetic flux emergence.

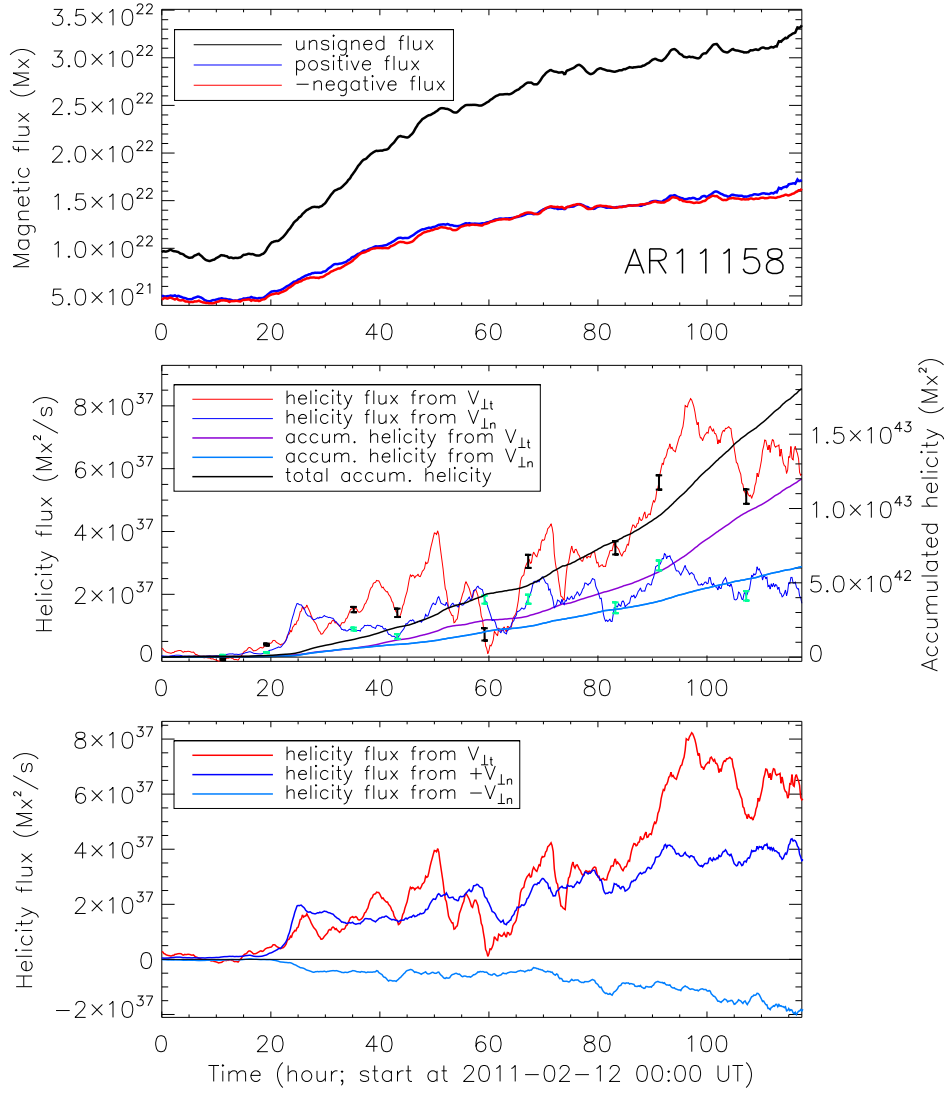


Fig. 12.— Same as in Fig.4 but for AR11158. The curves start at 00:00 UT 12 February 2011.

3.3. Summary and Discussion

We summarize our analysis for the two emerging active regions as follows. Magnetic energy (including both potential energy and free energy) in the corona was contributed mainly by the emergence-term. It contributes 61% of total energy for AR11072, and 62% for AR11158. The emergence- and shear-energy fluxes evolved consistently in phase during

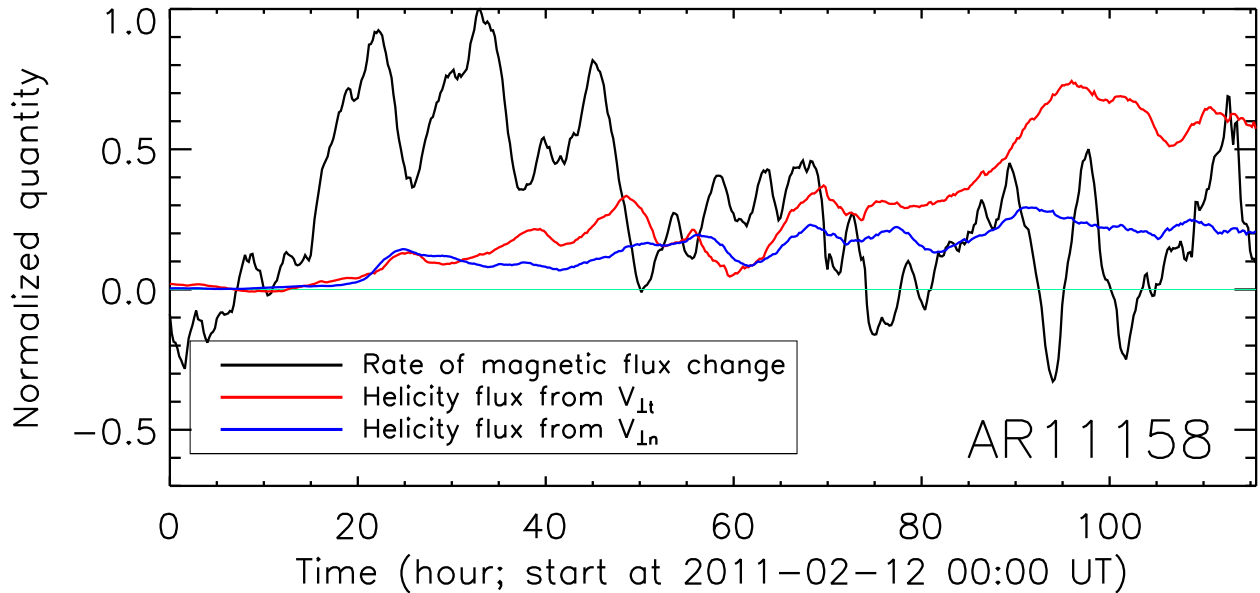


Fig. 13.— Same as in Fig.5 but for AR 11158.

the entire flux emergence course. Magnetic helicity in the corona, on the other hand, was contributed mainly by the shear-term. It contributes 88% of total helicity for AR 11072, and 66% for AR 11158. Both shear- and emergence-helicity fluxes have the same sign. If the emergence-helicity flux is separated into upflow-helicity flux (helicity flux from upflows) and downflow-helicity flux (helicity flux from downflows), the upflow-helicity flux was very low in AR 11072 during its entire emergence course, and was low in AR 11158 during its main flux emergence phase within hours 20–50.

As described in Section 1, magnetic helicity in the corona comes from normal flows that normally advect the twisted magnetic flux into the corona, and is generated by surface flows that shear and braid magnetic fields (e.g., Berger 1984; Kusano et al. 2002; Nindos et al. 2003; Pevtsov et al. 2003; Pariat et al. 2005; Démoulin 2007). With this interpretation, the helicity flux from upflows is deemed to be the helicity that is injected into the corona purely by flux emergence. The result that the shear-term outweighs the upflows in injecting helicity into the corona during the flux emergence suggests a two-stage scenario for buildup of helicity in the corona: at beginning, the magnetic field with low helicity emerges into the corona (the first stage); it is then sheared and twisted by surface shearing flows (the second stage) afterwards, which builds up most helicity in the corona. When the field is non-linear force-free, the *relative* helicity is found to have “a statistically robust, monotonic correlation” with the free magnetic energy in a sample of 42 active regions (Tziotziou et al. 2012). Thus the aforementioned scenario implies that the emerged field in these two active

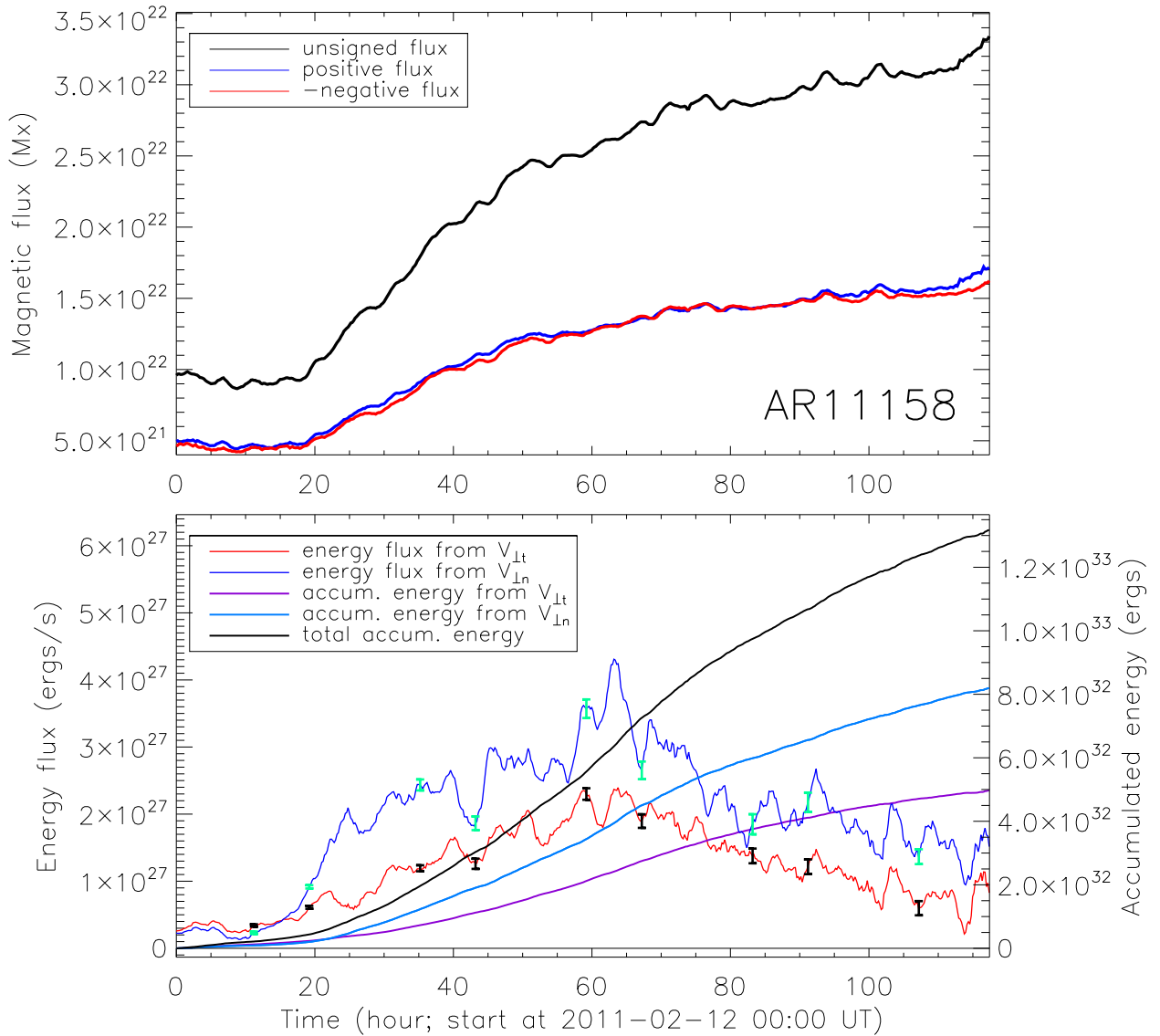


Fig. 14.— Same as in Fig. 6 but for AR11158. The curves start at 00:00 UT 12 February 2011.

regions studied initially contained less *free* energy. Much more *free* energy was built up later by the surface shearing flows. The surface flows are probably caused by the flux emergence, which will be discussed in next paragraph.

Longcope & Welsch (2000) proposed a dynamical model that suggests that only a fraction of the current carried by a twisted flux tube will pass into the corona. This leads to torsional Alfvén waves that propagate along the flux tube, transporting magnetic twist from the highly twisted portion of the flux tube under the photosphere to the less twisted portion

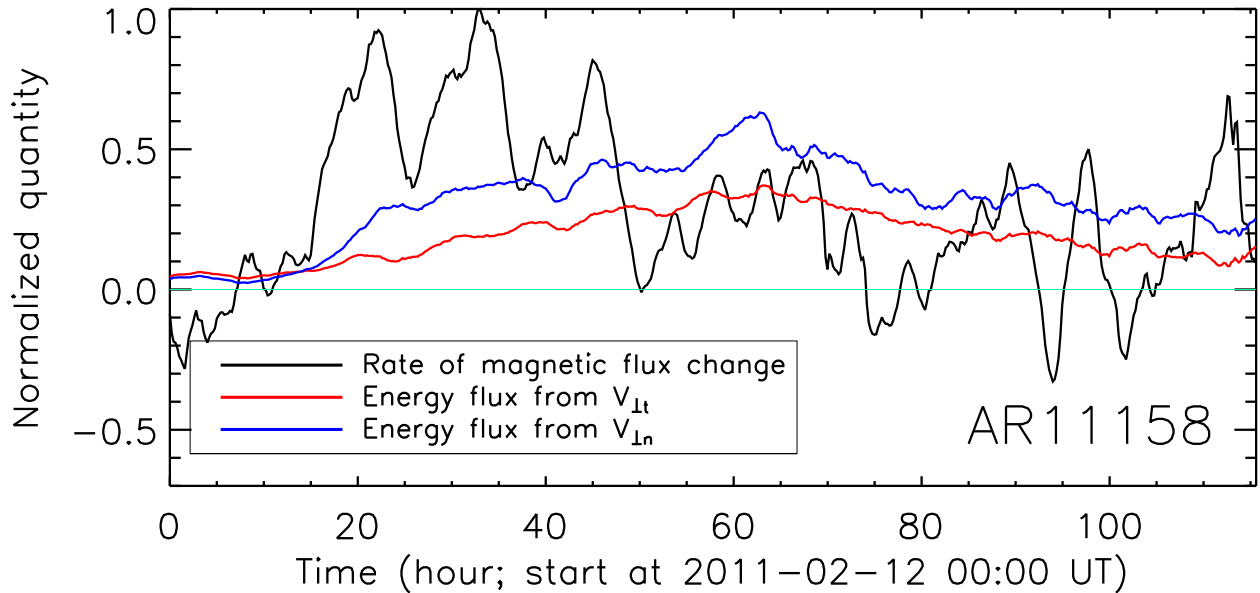


Fig. 15.— Same as in Fig. 7 but for AR 11158.

of the flux tube that emerged and expanded in the corona. This process is manifested on the photosphere with rotational motions of sunspots that are often observed in active regions during their emergence. Pevtsov et al. (2003) tested this model with six emerging active regions. They found reasonable agreement between the model prediction and observation. MHD simulations successfully reproduced the processes the model predicts (e.g. Magara & Longcope 2003; Fan 2009). More generally, a common feature from simulations of emergence of a highly twisted flux tube is that it is difficult for the flux tube to rise bodily into the corona entirely. Instead, only upper parts of the helical field lines of the twisted tube expand into the corona, and this emergence also causes surface flows (e.g. Fan & Gibson 2003; Magara & Longcope 2003; Manchester et al. 2004; Fan 2009; Cheung et al. 2010).

From helicity-injection point of view, this model predicts that a small amount of helicity is injected by emergence-term due to emergence of less twisted flux tubes. Much of the helicity is injected by the surface flows that twist and braid the emerged field lines afterwards. Thus the shear-helicity flux is dominant during the flux emergence. Indeed, the MHD simulations from Magara & Longcope (2003); Fan (2009) have demonstrated that the shear-term contributes most of helicity in the corona during flux emergence. This is consistent with the observational results shown in this study. A significant difference between the MHD simulations and our observational results is that, in the MHD simulations, there is a very short impulsive helicity injection from the emergence-term at the beginning of the flux emergence, which the observation did not have. The initial twist in the flux tube in these simulations is

set to be fairly high. Although the emerged part of the flux tube only has a fraction of initial twist, it still contains certain amount of electric current. Emergence of this current-carrying flux tube into the corona certainly injects a great amount of helicity that is reflected in the emergence-term, which leads to that short impulsive injection from the emergence-term. In the two active regions analyzed here, only low helicity injection but without that impulsive injection is measured from the emergence-term during their emergence. This may indicate that the emerged flux tubes are much less twisted at the beginning. Much of twist is built up later by the shearing flows.

Another interesting result in this study is that the coronal energy (including both potential energy and free energy) in the active regions is mainly contributed by the emergence-term during flux emergence. It agrees partly with what MHD simulations have predicted that emergence-term contributes substantial energy into the corona (Fan & Gibson 2003; Magara & Longcope 2003; Manchester et al. 2004; Wu et al. 2006; Cheung et al. 2010). However, the MHD simulations predicted that this emergence-term energy injection only takes place in early phase of flux emergence. In contrast, we found in AR 11072 that this energy injection lasted through the entire emergence course, and remained fairly high even after the emergence significantly reduced. The source of this energy injection was the areas surrounding the leading sunspot where strong upflows and tangential magnetic fields are found (see Figs. 8).

Decomposing the helicity flux into the emergence-term and the shear-term in emerging active regions have been studied before by, e.g., Kusano et al. (2002); Yamamoto et al. (2005); Yamamoto & Sakurai (2009); Zhang et al. (2012). Zhang et al. (2012) made use of the DB03-hypothesis that is demonstrated to be incorrect in next Section, and thus this work is excluded in this discussion. Kusano et al. (2002) combined the line-of-sight magnetograms taken by MDI and the vector magnetic field data taken by the vector magnetograph at NAOJ to study magnetic helicity and Poynting fluxes across the photosphere in an emerging active region, AR 8100. They applied a Local Correlation Tracking (LCT) technique to MDI magnetograms to derive tangential velocity, and then determined the normal velocity by solving the normal component of the induction equation with the vector magnetic field data and the aforementioned tangential velocity. They found that the photospheric shear motion and the flux emergence process equally contributed to the helicity injection and supplied magnetic helicity of opposite signs into the active region, and the energy flux from the emergence term was dominant in the active region. With the same method, Yamamoto et al. (2005); Yamamoto & Sakurai (2009) analyzed more active regions. They found in another emerging active region, AR 8011, that the helicity flux from the shear term first had the sign opposite to that from the emergence term, and later changed the sign. The fluxes from both terms were comparable. These results are opposite to what we found in this

study. Besides the limitation of the method they used and the caveats in the data used as mentioned in Section 1, such as outstanding data gaps, inconsistency of data quality due to seeing and other conditions, there are several other reasons that may cause this discrepancy. For example, using data from different instruments might need careful cross calibration, which is not trivial (Leka & Barnes 2012; Liu et al. 2012). The active regions analyzed in their studies and ours are obviously different, which may have different properties during their emergence. Further study is needed.

4. Test of DB03 Hypothesis

Démoulin & Berger (2003) conjectured that the geometry of magnetic field in the photosphere implies that the velocity derived by tracking magnetic footpoints (\mathbf{U} hereafter) is in fact the flux transport velocity. This way, the total helicity and energy fluxes across the photosphere can be computed by Equations (4)–(5). This hypothesis has been examined using a MHD simulation data (Schuck 2008). It is concluded that “line-of-sight tracking methods capture the shearing motion of magnetic footpoints but are insensitive to flux emergence—the velocities determined from line-of-sight methods are more consistent with tangential plasma velocities than with flux transport velocities.” Here we test this hypothesis using observational data from HMI.

We use a tracking algorithm, the differential affine velocity estimator (DAVE; Schuck 2006), to derive \mathbf{U} strictly from the evolution of just B_n . The data used are time-series normal magnetic field for AR 11072 and AR 11158 described in Section 2. Helicity and energy fluxes are then computed using Equations (4)–(5) (DAVE-helicity flux and DAVE-energy flux, hereafter). DB03 hypothesis predicts that DAVE-helicity flux should be equal to summation of DAVE4VM shear- and emergence-helicity fluxes, and DAVE-energy flux should be equal to summation of DAVE4VM shear- and emergence-energy fluxes, respectively. Plotted in the top panels of Figs. 16 and 17 are temporal profiles of shear- (red), emergence- (blue) and DAVE-helicity fluxes (light blue). The black curve represents the total helicity flux, summation of the shear- and emergence-helicity fluxes. The bottom panels are the same as in the top but for energy fluxes. The shear- and emergence-helicity and energy fluxes are calculated using velocity \mathbf{V}_\perp , the DAVE4VM-derived velocity with field-aligned plasma flows removed. In both cases, DAVE-helicity and energy fluxes do not equal the total helicity and energy fluxes estimated from DAVE4VM; to be fair, the DAVE-helicity tracks the total helicity fairly well though. DAVE-helicity flux is fairly close to the total helicity flux. It caught about 76% of the total helicity accumulated in the corona in that 6-day period for AR 11072, and 83% for AR 11158 in that 5-day period. DAVE-energy flux, on the other

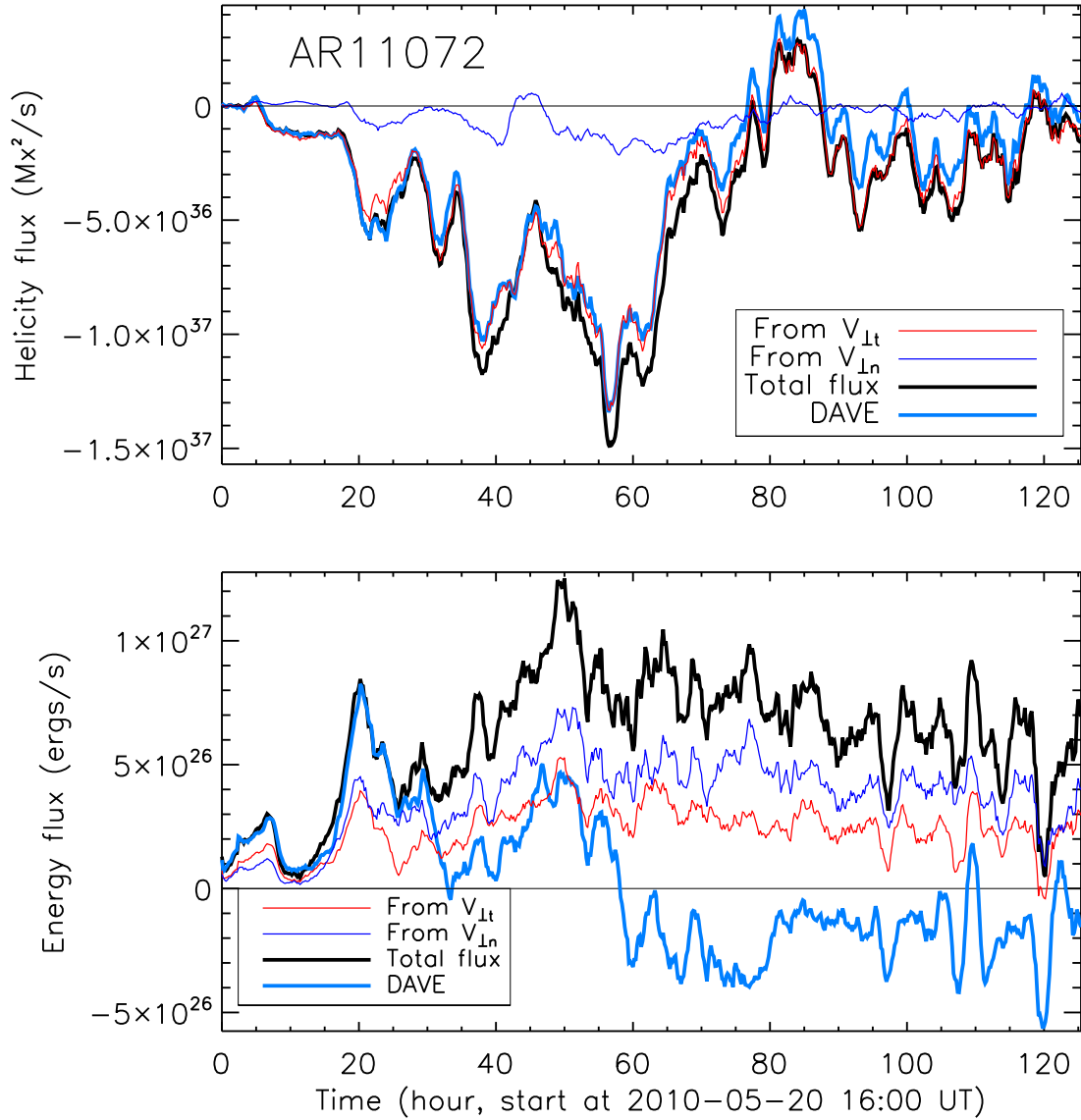


Fig. 16.— Top: Shear-helicity flux (red), emergence-helicity flux (blue), total of shear- and emergence-helicity fluxes (black), and DAVE-helicity flux (light blue) for AR11072, respectively. Bottom: same as that in the top panel but for energy flux.

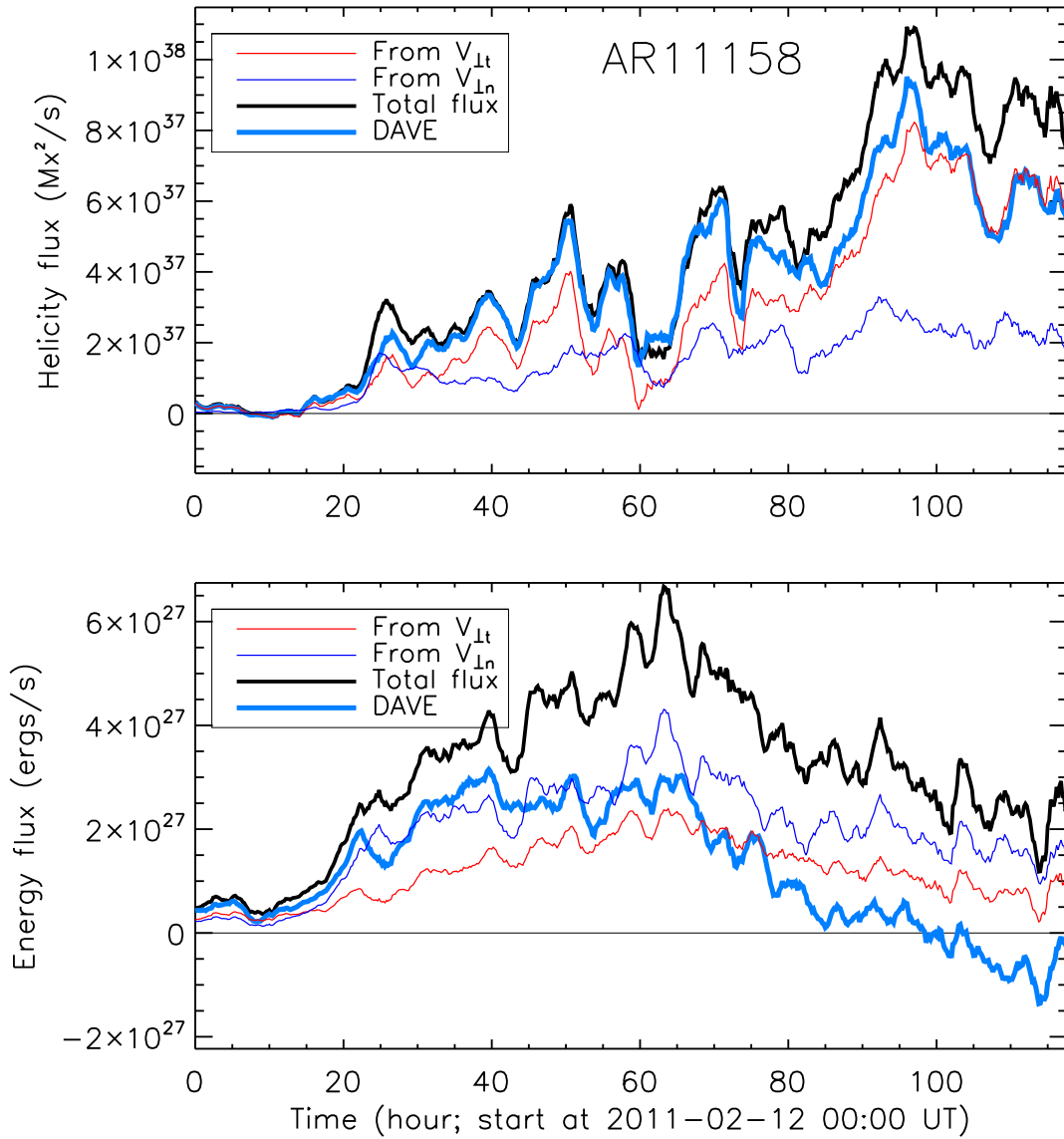


Fig. 17.— Same as Fig.16 but for AR 11158.

hand, is significantly different from the total energy flux. The DAVE-energy flux estimates captured only 3% of the total energy (estimated from DAVE4VM) for AR 11072, and 39%

for AR11158. The combined helicity and energy flux results disagree with the predictions of the DB03 hypothesis.

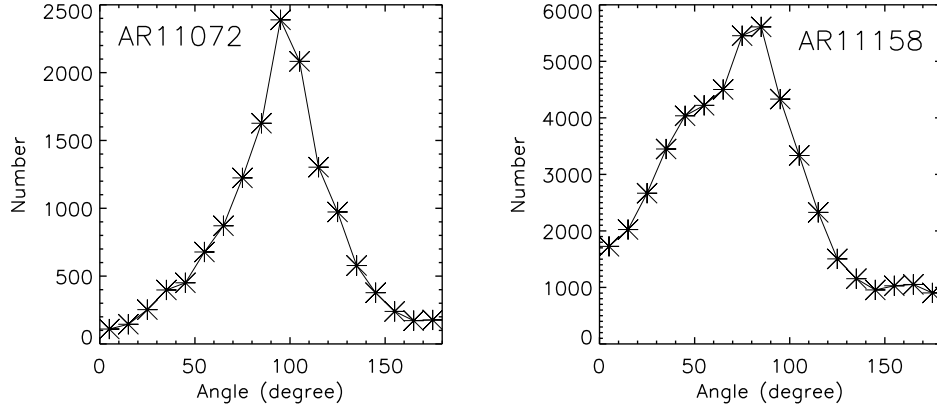


Fig. 18.— Distribution of the angle between \mathbf{A}_p and \mathbf{B}_t . Left: histogram of the angle for AR11072. The angle is computed using the vector magnetic field data taken at 12:00 UT 2010 May 22. Right: histogram of the angle for AR11158. The data used was taken at 19:48 UT 2011 February 14. Only pixels with \mathbf{B}_t greater than 100 Gauss are counted.

What is particularly interesting here is that for the DAVE4VM results, the helicity flux is largely determined by the shearing term

$$\left. \frac{dH}{dt} \right|_S = 2 \int_S (\mathbf{A}_p \cdot \mathbf{B}_t) V_{\perp n} dS - 2 \int_S (\mathbf{A}_p \cdot \mathbf{V}_{\perp t}) B_n dS \simeq -2 \int_S (\mathbf{A}_p \cdot \mathbf{V}_{\perp t}) B_n dS, \quad (8)$$

whereas for the energy flux, both terms are contributors while the emerging term dominates

$$\left. \frac{dE}{dt} \right|_S = \frac{1}{4\pi} \int_S B_t^2 V_{\perp n} dS - \frac{1}{4\pi} \int_S (\mathbf{B}_t \cdot \mathbf{V}_{\perp t}) B_n dS \sim \frac{1}{4\pi} \int_S B_t^2 V_{\perp n} dS. \quad (9)$$

Noting that $V_{\perp n}$ is non zero over much of the active region, Eqn. 8 implies that $\mathbf{A}_p \cdot \mathbf{B}_t \simeq 0$. Figure 18 shows distribution of the angle between \mathbf{A}_p and \mathbf{B}_t . In the left is a histogram of the angle for AR11072 using the vector magnetic field data taken at 12:00 UT 2010 May 22. In the right for AR11158 at 19:48 UT 2011 February 14. Only pixels with tangential field greater than 100 Gauss, roughly the noise level of the HMI vector field data (Hoeksema et al. 2012), are counted here. The median of the angle is 95° for AR11072, and 75° for AR11158. In both cases, the peaks of the distributions are close to 90° implying $\mathbf{A}_p \cdot \mathbf{B}_t \simeq 0$.

As another test, we directly used the total vector velocity derived by DAVE4VM, *without removing the field-aligned plasma flows*, to calculate the individual energy- and helicity-flux terms (this is technically incorrect for computing the individual terms). Plotted in

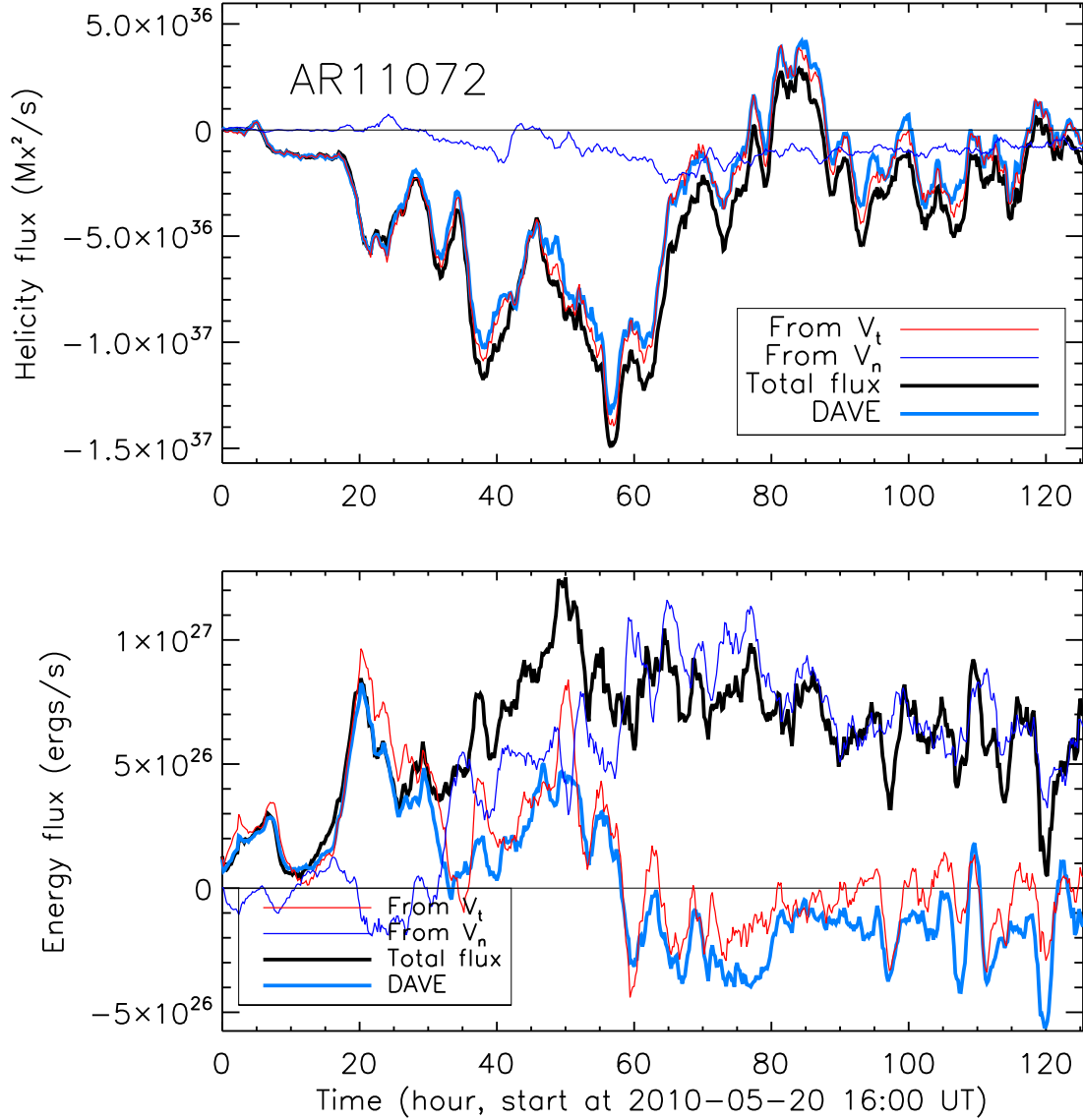


Fig. 19.— Top: \mathbf{V}_t -term helicity flux (red), \mathbf{V}_n -term helicity flux (blue), total of \mathbf{V}_t -term and \mathbf{V}_n -term helicity fluxes (black), and DAVE-helicity flux (light blue) for AR11072, respectively. Bottom: same as that in the top panel but for energy flux.

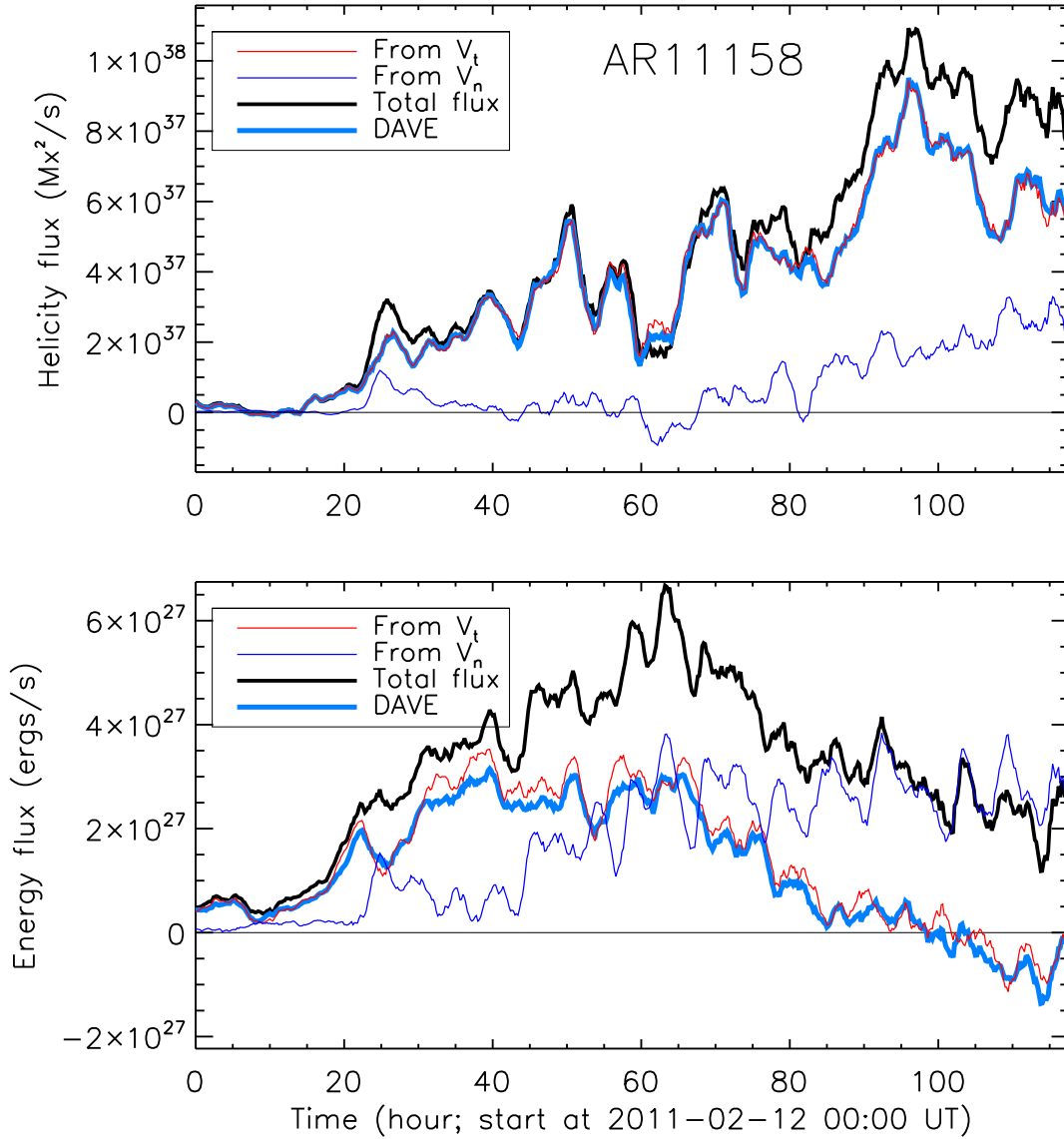


Fig. 20.— Same as Fig. 19, but for AR11158.

the top panels of Figs. 19 and 20 are temporal profiles of V_t -term (red), V_n -term (blue) and DAVE-helicity fluxes (light blue). The black curve represents the total helicity flux,

summation of the \mathbf{V}_t -term and \mathbf{V}_n -term helicity fluxes. The bottom panels are the same as in the top but for energy fluxes. \mathbf{V}_t and \mathbf{V}_n are tangential and normal components of velocity derived by DAVE4VM. Again, in both cases, DAVE-helicity and energy fluxes do not equal the total helicity and energy fluxes (which are identical to the total fluxes in Figs 16-17). Instead, DAVE-helicity and energy fluxes agree very well with \mathbf{V}_t -term helicity and energy fluxes. To be more quantitative, in another test, we calculated Pearson linear correlation coefficients between \mathbf{V}_t and $\mathbf{U}(\text{DAVE})$, and between $\mathbf{U}(\text{DAVE4VM})$ and $\mathbf{U}(\text{DAVE})$ for each active region. Here, $\mathbf{U}(\text{DAVE})$ denotes the tangential velocity inferred by DAVE, and $\mathbf{U}(\text{DAVE4VM})$ is the flux transport velocity computed by $\mathbf{U}(\text{DAVE4VM}) = \mathbf{V}_{\perp t} - \frac{V_{\perp n}}{B_n} \mathbf{B}_t$, where, $\mathbf{V}_{\perp t}$ and $V_{\perp n}$ are tangential and normal components of velocity V_{\perp} , derived by DAVE4VM with the field-aligned plasma flows removed. \mathbf{B}_t and B_n are tangential and normal fields. We also calculated the vector correlation coefficient and Cauchy-Schwarz inequality (Schrijver et al. 2006). Vector correlation coefficient is defined as,

$$C_{vec} = \frac{\sum_i \mathbf{V}_i \cdot \mathbf{U}_i}{(\sum_i \mathbf{V}_i^2 \sum_i \mathbf{U}_i^2)^{1/2}}, \quad (10)$$

where \mathbf{V}_i and \mathbf{U}_i are velocities at pixel i . Cauchy-Schwarz inequality is defined as,

$$C_{cs} = \frac{1}{M} \sum_i \frac{\mathbf{V}_i \cdot \mathbf{U}_i}{|\mathbf{V}_i| |\mathbf{U}_i|}, \quad (11)$$

where M is the total number of pixels in the region studied. Here we only use two components of vector velocity field, i.e., the tangential velocity, to compute C_{vec} and C_{cs} . The data used were taken at 12:00 UT 2010 May 22 for AR 11072, and at 19:48 UT 2011 February 14 for AR 11158. Only the pixels with the tangential and normal fields greater than 100 Gauss are selected for those computations. The result is shown in Table 1, where CC refers to Pearson linear correlation coefficient, C_{vec} denotes vector correlation coefficient defined by Eq. 10, and C_{cs} is Cauchy-Schwarz inequality defined by Eq. 11. It is shown that the coefficients between the \mathbf{V}_t and $\mathbf{U}(\text{DAVE})$ are much higher than those between $\mathbf{U}(\text{DAVE4VM})$ and $\mathbf{U}(\text{DAVE})$ in all measures. These further confirm the conclusion in Schuck (2008) that the velocities determined from tracking methods are more consistent with tangential plasma velocities than with flux transport velocities. These tangential plasma velocities contain the field-aligned plasma flows. Without vector magnetic field data, these flows cannot be removed to accurately compute the individual shearing and emergence contributions. Thus, the line-of-sight magnetograms cannot even be used to calculate the shear-term reliably.

5. Conclusions

Using HMI vector magnetic field data, we study magnetic helicity and energy in the corona in two emerging active regions, AR 11072 and AR 11158. The magnetic helicity and energy in the corona are calculated by integrating over time the helicity- and energy-fluxes across the photosphere. These fluxes consist of two components. One is from the photospheric shear motion (shear-term), and the other from emergence (emergence-term). The vector velocity field on the photosphere is derived by applying DAVE4VM to the time-series vector magnetic field data, and further corrected by removing the irrelevant field-aligned plasma flow. It is found that magnetic energy (including both potential energy and free energy) in the corona was contributed mainly by the emergence-term: for AR 11072, emergence-term contributes 61% of total energy; for AR 11158, it is 62%. During the entire emergence course, the emergence-energy flux is higher than the shear-energy flux, and both fluxes evolved consistently in phase. In AR 11072, the emergence-energy flux remained fairly high after the flux emergence became much less significant. The source of this energy injection was the areas surrounding the leading sunspot, where strong upflows and tangential magnetic field were observed.

Magnetic helicity in the corona was contributed mainly by the shear-term. For AR 11072, it contributes about 88% of total helicity; for AR 11158, it is 66%. Both shear- and emergence-helicity fluxes have the same sign. The helicity flux from upflows was very low in AR 11072 during its entire emergence, and low in AR 11158 during its main flux emergence phase. This implies that the emerged field initially contained low helicity. Much more helicity was built up afterwards by the photospheric shearing flows that twisted and braided the field lines, which is supported by the result that the shear-term contributed most helicity in the corona. When magnetic field is force-free, it is found that there is a monotonic correlation between the magnetic helicity and free energy (Tziotziou et al. 2012). Thus, the aforementioned results imply that the *free* magnetic energy is initially low in the emerged magnetic field, much of *free* energy is built up later by the shearing flows.

Using HMI data, we also examine Demoulin & Berger’s hypothesis (2003). The test shows that the helicity- and energy-fluxes calculated from the apparent tangential velocity derived by tracking the footpoints of magnetic field are consistent with those from the tangential plasma velocity, but do not equal the total fluxes as predicted by the hypothesis. This further confirms the conclusion in Schuck (2008) that the velocities determined from simple tracking methods such as LCT and DAVE are more consistent with tangential plasma velocities than with flux transport velocities. In the two emerging active regions studied here, the helicity in the corona was mainly contributed by the tangential flows. Therefore the helicity computed from the tracking velocity is considered to be a fairly good approximation of the

total helicity. The energy is significantly different, however.

We wish to thank the team members who have made great contributions to this SDO mission for their hard work! We also wish to thank the anonymous referees for their critical comments which help improve this work. This work was supported by NASA Contract NAS5-02139 (HMI) to Stanford University. The data have been used by courtesy of NASA/SDO and the HMI science team.

REFERENCES

- Berger, M. A. 1984, *Geophysical & Astrophysical Fluid Dynamics*, 30, 79
- . 1997, *Journal of Geophysical Research*, 102, 2637
- Berger, M. A., & Field, G. B. 1984, *J. Fluid Mech.*, 147, 133
- Berger, M. A., & Ruzmaikin, A. 2000, *Journal of Geophysical Research*, 105, 10481
- Borrero, J. H., Tomczyk, S., Kubo, M., Socas-Navarro, H., Schou, J., Couvidat, S., & Bogart, R. 2011, *Sol. Phys.*, 273, 267
- Cheung, M. C. M., Rempel, M., Title, A. M., & Schüssler, M. 2010, *Astrophys. J.*, 720, 233
- Démoulin, P. 2007, *Advances in Space Research*, 39, 1674
- Démoulin, P., & Berger, M. A. 2003, *Sol. Phys.*, 215, 203
- Démoulin, P., & Pariat, E. 2009, *Advances in Space Research*, 43, 1013
- DeRosa, M. L., et al. 2009, *Astrophys. J.*, 696, 1780
- Fan, Y. 2009, *Astrophys. J.*, 697, 1529
- Fan, Y., & Gibson, S. E. 2003, *Astrophys. J.*, 589, L105
- Georgoulis, M. K., & LaBonte, B. J. 2006, *Astrophys. J.*, 636, 475
- Hoeksema, J. T., et al. 2012, *Sol. Phys.*, in preparation
- Jing, J., Park, S., Liu, C., Lee, J., Wiegmann, T., Xu, Y., Deng, N., & Wang, H. 2012, *Astrophys. J. Lett.*, 752, article id. L9

- Klimchuk, J. A., & Canfield, R. C. 1994, in ASPC Series, Vol. 68, Solar active region evolution: comparing models with observations, 233
- Kusano, K., Maeshiro, T., Yokoyama, T., & Sakurai, T. 2002, *Astrophys. J.*, 577, 501
- Leka, K. D., & Barnes, G. 2012, *Sol. Phys.*, 277, 89
- Leka, K. D., Barnes, G., Crouch, A. D., Metcalf, T. R., Gary, G. A., Jing, J., & Liu, Y. 2009, *Sol. Phys.*, 260, 83
- Liu, Y., & Schuck, P. W. 2012, *Sol. Phys.*, submitted
- Liu, Y., et al. 2012, *Sol. Phys.*, 279, 295
- Longcope, D. W. 2004, *Astrophys. J.*, 612, 1181
- Longcope, D. W., & Welsch, B. T. 2000, *Astrophys. J.*, 545, 1089
- Magara, T., & Longcope, D. W. 2003, *Astrophys. J.*, 586, 630
- Manchester, W. I., Gombosi, T., DeZeeuw, D., & Fan, Y. 2004, *Astrophys. J.*, 610, 588
- Metcalf, T. R. 1994, *Sol. Phys.*, 155, 235
- Metcalf, T. R., Jiao, L., McClymont, A. N., Canfield, R. C., & Ultenbroek, H. 1995, *Astrophys. J.*, 439, 474
- Metcalf, T. R., et al. 2006, *Sol. Phys.*, 237, 267
- Nindos, A., Zhang, J., & Zhang, H. 2003, *Astrophys. J.*, 594, 1033
- Norton, A. A., et al. 2006, *Sol. Phys.*, 239, 69
- Pariat, E., Démoulin, P., & Berger, A. A. 2005, *Astronomy and Astrophysics*, 439, 1191
- Pariat, E., Nindos, A., Démoulin, P., & Berger, A. A. 2006, *Astronomy and Astrophysics*, 452, 623
- Pesnell, P. D., Thompson, B. J., & Chamberlin, P. C. 2012, *Sol. Phys.*, 275, 3
- Pevtsov, A. A., Maleev, V. M., & Longcope, D. W. 2003, *Astrophys. J.*, 593, 1217
- Ravindra, B., Longcope, D. W., & Abbett, W. P. 2008, *Astrophys. J.*, 677, 751
- Régnier, S., & Canfield, R. C. 2006, *Astron. Astrophys.*, 451, 319

- Scherrer, P. H., et al. 1995, *Sol. Phys.*, 162, 129
- . 2012, *Sol. Phys.*, 275, 207
- Schou, J., et al. 2012, *Sol. Phys.*, 275, 229
- Schrijver, C. J., et al. 2006, *Sol. Phys.*, 235, 161
- Schuck, P. W. 2006, *Astrophys. J.*, 646, 1358
- . 2008, *Astrophys. J.*, 683, 1134
- Sun, X., Hoeksema, J. T., Liu, Y., Wiegelmann, T., Hayashi, K., Chen, Q., & Thalmann, J. 2012, *Astrophys. J.*, 748, article id. 77
- Tian, L., & Alexander, D. 2008, *Astrophys. J.*, 673, 532
- Turmon, M., Jones, H. P., Malanushenko, O. V., & Pap, J. M. 2010, *Sol. Phys.*, 262, 277
- Tziotziou, K., Georgoulis, M. K., & Raouafi, N.-E. 2012, *Astrophys. J. Lett.*, in press
- Wang, S., Liu, C., Liu, R., Deng, N., Liu, Y., & Wang, H. 2012, *Astrophys. J. Lett.*, 745, article id. L17
- Welsch, B. T., Fisher, G. H., Abbett, W. P., & Régnier, S. 2004, *Astrophys. J.*, 610, 1148
- Welsch, B. T., et al. 2007, *Astrophys. J.*, 670, 1434
- Wu, S. T., Wang, A. H., Liu, Y., & Hoeksema, J. T. 2006, *Astrophys. J.*, 652, 800
- Yamamoto, T. T., Kusano, K., Maeshiro, T., Yokoyama, T., & Sakurai, T. 2005, *Astrophys. J.*, 624, 1072
- Yamamoto, T. T., & Sakurai, T. 2009, *Astrophys. J.*, 698, 928
- Zhang, Y., Kitai, R., & Takizawa, K. 2012, *Astrophys. J.*, 751, article id. 85

Table 1. Comparison of different velocities. \mathbf{V}_t and \mathbf{V}_n in the second column denote the tangential and normal velocities derived by DAVE4VM. \mathbf{U} (DAVE) is the tangential velocity derived by DAVE. \mathbf{U} (DAVE4VM) is the flux transport velocity computed by $\mathbf{U}(\text{DAVE4VM}) = \mathbf{V}_{\perp t} - \frac{V_{\perp n}}{B_n} \mathbf{B}_t$, where, $\mathbf{V}_{\perp t}$ and $V_{\perp n}$ are tangential and normal components of velocity V_{\perp} , derived by DAVE4VM with the field-aligned plasma flows removed. \mathbf{B}_t and B_n are tangential and normal fields. CC represents the Pearson linear correlation coefficients between different velocities in x-axis (the third column) and y-axis (the fourth column). C_{vec} and C_{cs} in columns 5 and 6 refer to the vector correlation coefficient and the Cauchy-Schwarz inequality, respectively.

Active Region	Comparison	CC [V_x]	CC [V_y]	C_{vec}	C_{cs}
AR11072	\mathbf{V}_t vs \mathbf{U} (DAVE)	0.98	0.96	0.97	0.95
AR11072	\mathbf{U} (DAVE4VM) vs \mathbf{U} (DAVE)	0.78	0.77	0.79	0.87
AR11158	\mathbf{V}_t vs \mathbf{U} (DAVE)	0.98	0.98	0.98	0.95
AR11158	\mathbf{U} (DAVE4VM) vs \mathbf{U} (DAVE)	0.76	0.70	0.73	0.81